The effect of ambient pressure on the subharmonic acoustic response of monodisperse microbubbles

Wilmer Schroer, *w.schroer@student.utwente.nl*, s1861085, BME

May 2022

Abstract

In this thesis, the effect of the ambient pressure on the acoustic response of three different kinds of monodisperse microbubbles, with different phospholipid shell stiffness was studied. The shell stiffness was modified by adding different molar fractions of palmatic acid to the shell. Using a Verasonics Vantage research ultrasound system and the P4-1 ultrasound probe, both the fundamental and subharmonic mean power of the scattered bubble signal during an ambient pressure increase was investigated. A new variable, the Corrected Change of Subharmonic (CCoS) is introduced to combine both the fundamental and subharmonic scattered behaviour of the bubbles into a single variable in order to make hydrostatic pressure estimations of the medium surrounding the bubbles. The results show that increasing the stiffness of the shell of lipid coated microbubbles significantly increases measured values of the CCoS. This increase is caused by both the changed attenuation spectra of the bubbles at low acoustic pressures, as well as the change in acoustic response of the bubbles due to increasing stiffness. The resolution of the hydrostatic pressure estimation is still insufficient for clinical applications, but the method shows promising results and, in the future, might be a clinically viable alternative to current methods.

Contents

1 Introduction

Accurate local hydrostatic pressure measurements in human patients for the diagnosis and treatment of a variety of diseases are of great value.[1] Currently, the golden standard for measuring the local hydrostatic pressure inside a vein or artery is catheterization, where a probe containing a pressure sensor is inserted into a body cavity, vein or artery. This procedure is not without risk[2] and can be very uncomfortable for the patient. Therefore, there is a need for a non-invasive method of determining the local hydrostatic pressure inside human patients.

The use of ultrasound contrast agents (UCAs) have been proposed as an alternative method.[3] It has been over two decades since the first UCAs have been approved for clinical use (Optison, 1998[4]). Since then, multiple other UCAs have been approved for clinical use (Sonazoid,[5] SonoVue[6] and more), all with the same goal of enhancing contrast in ultrasound imaging. UCAs are composed of microbubbles filled with an inert gas and have radii between $1 - 5$ µm, encapsulated by a surfactant. The surfactant lowers the surface tension between the bubble and the surrounding medium, causing the gas bubble to stabilize against dissolution into the surrounding medium. Due to the high compressibility of a gas versus that of liquid, UCAs naturally scatter ultrasound with an extremely high intensity with respect to blood. This effect is utilized in Contrast Enhanced UltraSound (CEUS), where a high concentration of an UCA is introduced into the blood flow, which lights up on an ultrasound image. An example of this is shown in Figure 1, where the contrast of the blood pool around a human liver is enhanced using the UCA SonoVue.

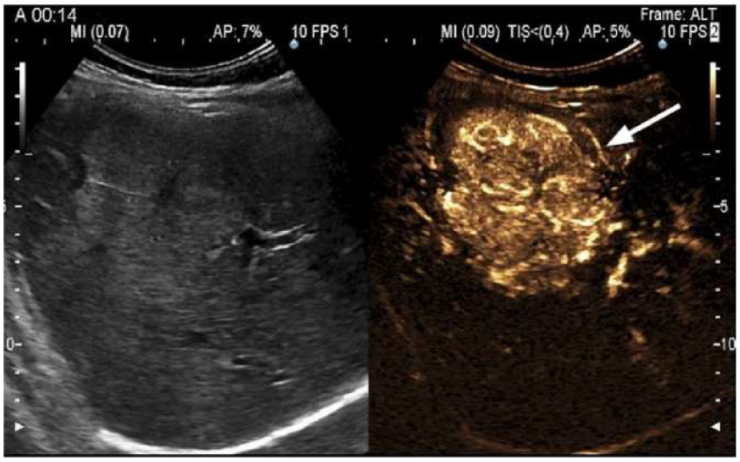

Figure 1: **UCA blood pool enhancement.** The liver of a 36-year-old woman before (left) and 15 seconds after SonoVue injection (right). Spoke-wheel-like enhancement of the arteries and veins can be observed.[7]

CEUS utilizes the principle of bubble resonance. Whenever a microbubble

of radius R_0 is irradiated with an ultrasound pulse with acoustic pressure P and frequency f, the radius of the bubble will start oscillating with frequency f. An oversimplified example: whenever the acoustic pressure of the ultrasound pulse increases, the bubble shrinks. Whenever the acoustic pressure decreases, the bubble expands. In reality, frequency dependent phaseshift makes this more complex, since at high frequencies the radial oscillation lags behind the pressure oscillation. The oversimplified effect is visualized in Figure 2 A. The oscillating bubble causes a secondary ultrasound field, scattered in all directions. This secondary scattered ultrasound field can then be received by the ultrasound transducer.

Depending on the bubble radius R_0, there is a frequency where the bubble absorbs and re-radiates most acoustic energy: the resonance frequency. when bubbles are driven at resonance frequency (or a multiple of the resonance frequency), their oscillations can be highly non-linear. This means that the scattered ultrasound field contains not only the resonance frequency f, but also higher harmonics (nf) and a subharmonic[8] (f/n, Figure 2 B). When a cloud of polydisperse bubbles is driven by a pulse, only a small fraction of these bubbles will be driven at resonance frequency. When driving a cloud of monodisperse microbubbles, all bubbles are being driven at resonance, which reduces the noice induced by non-resonant bubbles, increasing the signal to noise ratio.

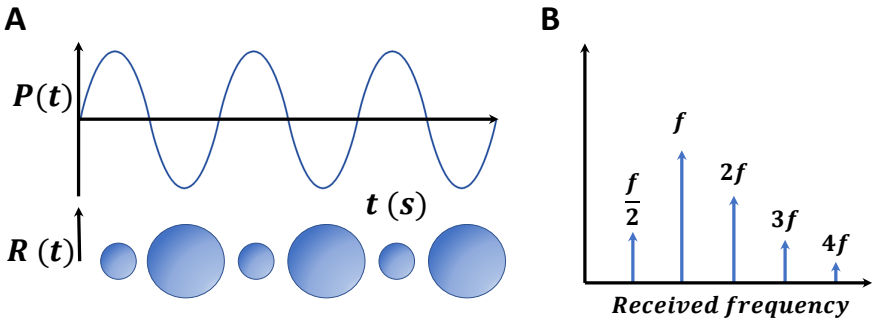

Figure 2: **Effects on a bubble and its scattered field by an ultrasound pulse. A:** Bubble oscillation due to an external ultrasound pulse. At maximum P, the radius of the bubble is at its minimum. At minimum P, the radius of the bubble is at its maximum. **B:** Frequency components of scattered ultrasound field emitted by a bubble driven at resonance frequency.

These harmonic and subharmonic responses have been proposed as an alternative method to measure the local hydrostatic pressure non-invasively. The subharmonic response of an microbubble has a strong dependence on the ambient pressure surrounding the microbubble.[9] Depending on the UCA and experimental properties, the subharmonic response can display a strong increase[10] or decrease[11] when the ambient pressure increases. This strong change

in intensity of the subharmonic response dependent on the ambient pressure can be utilized to estimate the ambient pressure in a system, as shown in the proof of concept by Forsberg.[3] Here, after injection of microbubbles, the aortas of two dogs were scanned with an experimental system by sending ultrasound pulses at 4 MHz, and receiving at 2 MHz. An algorithm was used in order to couple the received subharmonic frequency to an ambient pressure estimation. Forsberg was able to determine ambient pressure estimates that agreed reasonably well with those measured with pressure catheterization. Since then, there has been more research into understanding the subharmonic response of microbubbles. However, the pressure resolution that the subharmonic response of microbubbles offer still needs to be improved in order to meet clinical diagnostic requirements.[11] One example is the detection of portal hypertension, which is an increase in pressure within the portal vein. This vein carries blood from the digestive organs to the liver. Increased pressure in the portal vein causes large secondary veins to develop across the stomach, which can become fragile and bleed easily. Portal hypertension can be diagnosed with a local blood pressure measurement in the portal vein. In order to make an accurate diagnosis, a resolution of $\pm$ 5 mmHg is required.[12]

In this thesis, the goal is to test the effect of increasing shell stiffness and maximize the resolution of the ambient-pressure dependent subharmonic signal. This is done by creating three different types of monodisperse microbubbles. Each type of microbubble will have a different shell, and for each type of bubble, the optimal concentration for maximum ambient pressure sensitivity will be investigated. This will all be done by utilizing a Verasonics Vantage Research ultrasound system in combination with the medically relevant P4-1 ultrasound probe. This probe will be used to acoustically drive a bubble cloud located several centimeters from the transducer, on which an extra ambient pressure of up to 250 mmHg can be applied.

2 Background information

In this chapter, theoretical background information on monodisperse microbubbles, the effect of different bubble shells on the bubble properties and acoustical response, as well as how this theory combines with ambient pressure is given. This chapter is divided into three main sections: Bubble modelling, Lipid coated microbubbles and subharmonic response and the influence of ambient pressure. In the first section, a general model to describe the dynamics of phospholipid coated microbubbles will be introduced. In the second section, the physical and practical effects of encapsulating microbubbles with a lipid monolayer on the bubble properties will be discussed. In the final section, the subharmonic bubble response and its dependence on the ambient pressure will be discussed.

2.1 Bubble modelling

A general description of the dynamics of phospholipid coated microbubles is given by Marmottant *et al.* in the following Rayleigh-Plesset type of equation,[13]

$$\begin{aligned}\rho\Big(R\ddot{R}+\frac{3}{2}\dot{R}^2\Big) = \Big(P_0+\frac{2\sigma(R_0)}{R_0}\Big)\Big(\frac{R_0}{R}\Big)^{3\kappa}\Big(1-\frac{3\kappa\dot{R}}{c}\Big) \\ ... - \frac{2\sigma(R)}{R} - 4\mu\frac{\dot{R}}{R} - 4\kappa_{\mathrm{s}}\frac{\dot{R}}{R^2} - P_0 - P_{\mathrm{A}}(\mathrm{t}),\end{aligned} \tag{1}$$

where R is the spherical bubble radius, $\dot{R}$ and $\ddot{R}$ are the first and second order time derivative of the bubble radius R, R_0 the initial bubble radius, ρ the liquid density, μ the liquid viscosity, c the speed of sound in the medium, κ_{s} the surface dilatational viscosity, κ the polytropic exponent of the gas, P_0 the ambient pressure, $P_{\mathrm{A}}(t)$ the acoustic pressure and $\sigma(R)$ the interfacial surface tension between the bubble and its surroundings.
In order to incorporate the increase in ambient pressure that will be applied, P_0 will be substituted by:

$$P_0 = (P_{\mathrm{atm}} + P_{\mathrm{ov}}), \tag{2}$$

where P_{atm} is the atmospheric pressure, and P_{ov} the applied overpressure. In Equation 1, the surface tension $\sigma(R)$ has a dependence on the bubble radius. The widespread accepted breakthrough in modelling the non-linear dynamics of the bubble shell came from Marmottant *et al.*[13] Marmottant suggested that the radius the bubble can have is divided into three domains: $R_{\mathrm{buckled}}, R_{\mathrm{elastic}}$ and R_{ruptured}. In the buckled domain R_{buckled}, the surface tension is zero, while in the ruptured domain R_{ruptured}, the surface tension is that of the surrouding mediumm, in this case water. In between these two constant domains lies the elastic domain. In this domain, the surface tension scales linearly with the

bubble radius. In equation form, the Marmottant model is described as:

$$\sigma(R) = \begin{cases} 0 \text{ if } R \leq R_{\text{buckling}}, \\ \chi\left(\frac{R^2}{R_{\text{buckling}}^2} - 1\right) \text{ if } R_{\text{buckling}} \leq R \leq R_{\text{ruptured}}, \\ \sigma_{\text{water}} \text{ if ruptured and } R \geq R_{\text{ruptured}}, \end{cases} \tag{3}$$

where χ is the shell elasticity. This set of equations can be easily visualized for any type of lipid coated bubble when the surface area (and thus radius) of the bubble is non-dimensionalized with the initial surface area (and thus initial radius) of the bubble. During creation of the bubbles, the number of lipids in the bubble shell is fixed. After creation the bubble stabilizes by shrinking until the initial surface tension is low enough to form an equilibrium.[14] Following the Marmottant model, this initial surface tension σ_0 is then coupled to an initial surface area A_0. The initial surface tension effects both the fundamental and harmonic acoustical responses of the bubbles. The Marmottant model, together with a visualization of the three bubble domains, is displayed in Figure 3.

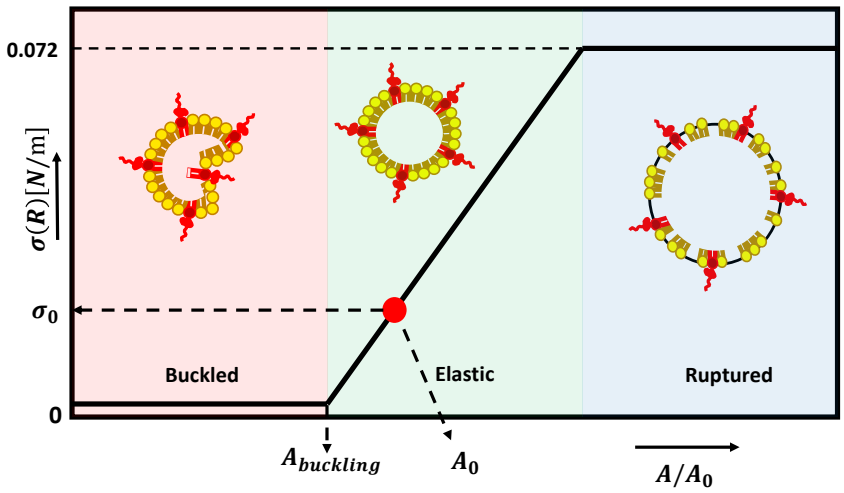

Figure 3: **The original Marmottant model for the dynamic surface tension of a monolayer coated microbubble.** At initial surface area A_0, the fixed number of lipids on the shell are at an equilibrium state, where there is an initial surface tension σ_0. Compression of the bubble causes buckling at bubble surface area A_{buckling}

.

The Marmottant model has been widely accepted to describe the acoustical response of a lipid monolayer-coated bubble. Sijl *et al.* proved that the model perfectly predicts so called 'compression-only' behaviour, which is thought to be an essential part of the subharmonic bubble response. In the paper, Sijl *et al.* perform a weak non-linear analysis, from which the following expression of

the effective shell stiffness results:

$$\chi_{\text{eff}} = \frac{1}{2} R_0 \frac{\partial \sigma(R)}{\partial R}\Big|_{R_0}, \tag{4}$$

which indicates that the effective shell elasticity is directly related to the slope of the surface tension curve in Marmottants model. However, the model is not perfect, since it predicts a perfectly linear surface tension curve, while later in this chapter it is shown that the surface tension does not follow a perfectly linear curve.

Changing the ambient pressure statically changes the radius of the bubble, which is important since the radius of the bubble is directly related to the surface tension described by Marmottant. At static condition ($\ddot{R} = 0, \dot{R} = 0$), the pressure inside a microbubble is higher than the ambient pressure. This is shown by the La place pressure, which for a bubble at zero overpressure gives:

$$P^0_{\text{G}_0} = p_{\text{atm}} + \frac{2\sigma_0}{R^0_0}, \tag{5}$$

where the superscript 0 indicates zero overpressure. Assuming that the gas content of the bubble remains constant, increasing the ambient pressure by applying overpressure leads to:

$$P_{\text{G}_0} = p_{\text{atm}} + p_{\text{ov}} + \frac{2\sigma}{R_0}, \tag{6}$$

(5) can be substituted into the polytropic gas law, which describes the gas pressure inside a bubble:

$$P_{\text{G}} = P_{\text{G}_0}\Big(\frac{R_0}{R}\Big)^{3\kappa}, \tag{7}$$

which gives:

$$P_{\text{G}_0} = \Big(p_{\text{atm}} + \frac{2\sigma_0}{R^0_0}\Big)\Big(\frac{R^0_0}{R_0}\Big)^{3\kappa}, \tag{8}$$

Equating expression(6) with (8) gives a solvable expression:

$$\Big(p_{\text{atm}} + \frac{2\sigma_0}{R^0_0}\Big)\Big(\frac{R^0_0}{R_0}\Big)^{3\kappa} = p_{\text{atm}} + p_{\text{ov}} + \frac{2\sigma}{R_0}, \tag{9}$$

from which the initial radius R_0 at the ambient static pressure $p_{\text{atm}} + p_{\text{ov}}$ can be obtained. This new radius also results in a new equilibrium surface tension, since compressing the bubble will decrease the dimensionless surface area of the bubble in the Marmottant model, leading to a decrease of the surface tension. Increasing the ambient pressure also results in isothermal compression of the gas inside the bubble. This results in a higher gas density in the bubble, which also has to be taken into account.

2.2 Lipid coated microbubbles

The lipids that were used to create monodisperse microbubbles were 1,2-distearoyl-sn-glycero-3-phosphocholine (DSPC), a PEGylated phospholipid 1,2-dipalmitoryl-sn-glycero-3-phosphoethanolamine conjugated polyethylene glycol (DPPE-PEG5000). Both these lipids are amphiphilic, which means that they have an hydrophobic tail and an hydrophilic head. This amphiphilic behaviour ensures that the lipids self-assemble at the surface of a bubble during formation in the bubble maker. A schematic representation of this self-assembled monolayer is displayed in Figure 4 A. As displayed in this figure, DPPE-PEG5000 (red) contains a large polyethylene glycol chain which aids in bubble stability during creation by preventing Ostwald ripening. The large chain forms a barrier between individual bubbles, ensuring they don't coalesce.[15]

The lipid monolayer forms a shell around the gas microbubble. This shell introduces a shell viscosity and shell elasticity to the bubble, which both effect the resonance frequency of a lipid coated microbubble:[16]

$$f_0 = \frac{1}{2\pi}\sqrt{\frac{1}{\rho R_0^2}\left(3\kappa_s P_0 + (3\kappa_s - 1)\frac{2\sigma(R_0)}{R_0} + \frac{4\chi}{R_0}\right)} \tag{10}$$

Both an increase in the shell elasticity χ and in increase in the shell viscosity κ_s affect the resonance frequency of the bubble, with the shell elasticity increasing the resonance frequency and the shell viscosity decreasing the resonance frequency. The shell elasticity χ is purely dependent on the packing density of the particles in the shell.[16] In a Langmuir Trough experiment it was proven that by adding smaller amphiphilic particles, the packing density of the particles in a lipid monolayer can be increased, thus increasing the elasticity of the monolayer.[17] It is believed that for microbubbles, the effect of adding small amphiphilic particles to the bubble shell results in the same increasing of the shell elasticity. Here, this is done by adding a certain mol% palmitic acid to the lipid mixture. This results in a more densely packed monolayer shell. An example with a low mol% palmitic acid is displayed in Figure 4 B.

The specific effect on the elasticity of adding palmitic acid to the bubble shell has been investigated by van Elburg,[18] and is shared with permission here. Figure 5 A shows the microbubble shell elasticity χ as function of the radius for different mol% PA concentrations in the microbubble shell. It can be observed that the shell elasticity is independent of the bubble radius R, which also means that this measured χ is equal to χ_{eff} of equation 4.

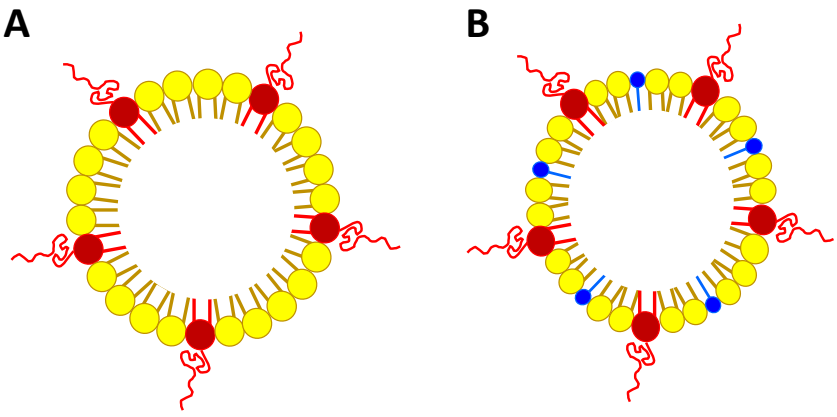

Figure 4: **Representation of microbubbles coated by a monolayer of lipids. A:** Lipid monolayer containing DSPC (yellow) and DPPE-PEG5000 (red) **B:** Lipid monolayer containing DSPC (yellow), DPPE-PEG5000 (red) and PA (blue).

Figure 5 B shows the microbubble shell elasticity as a function of palmitic acid concentration. As the mol% PA increases, the shell elasticity increases up until 50% PA. From this molar fraction onwards, the microbubbles are reported to become unstable, and the shell elasticity rapidly decreases.

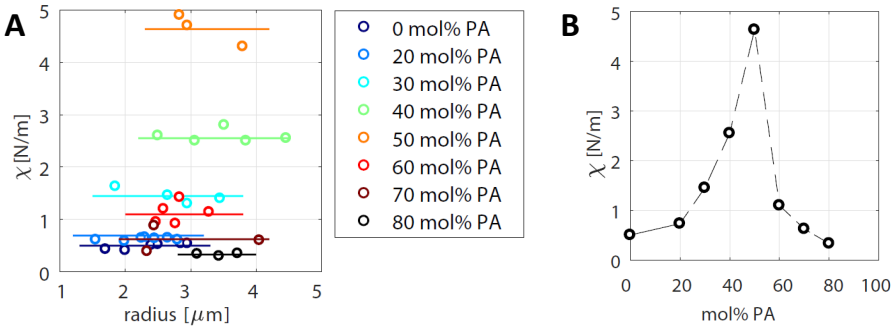

Figure 5: **Microbubble shell elasticity as function of bubble radius R and mol% PA. A:** Shell elasticity as function of radius for different mol% PA bubbles. Bubble elasticity is shown to be independent of bubble radius. **B:** Shell elasticity as function of mol% PA. The elasticity increases up until a maximum at 50% PA is reached. From EchoContrast 2021,[18] copied with permission.

Since χ is equal to χ_{eff} of equation 4, it is expected that high-elasticity bubble shells will result in a steeper slope of the surface tension curve with respect to the nondimensionalized bubble surface area. The surface tension curves of three

different bubbles were obtained using the method from Segers *et al.*[16] by van Elburg, and is displayed in Figure 6. These curves show an increase of surface tension slope as the mol% Pa increases. This increase in slope is expected to cause an increase in scattered subharmonic power.[19]

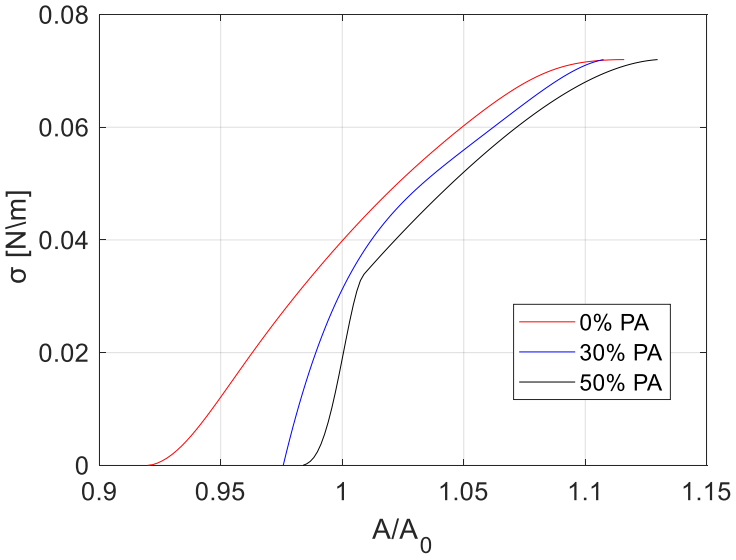

Figure 6: **Three different interfacial surface tension curves obtained using the method described by Segers et al[16]**. As the percentage of palmitic acid in the shell increases, the elasticity increases, which in turn results in a higher derivative of the surface tension. 50% PA (black) has a higher derivative than 30% PA (blue), which has a higher derivative than 0% PA (red). Here, we assume that the curve of the 50% PA is equal to the curve of 45% PA.
.

The monodisperse microbubbles are filled with perfluorbutane (C_4F_{10}). C_4F_{10} is an inert gas with a low aqueous solubility and diffusivity. This means that the bubbles predominantly maintain their gas volume when dissolved in liquids. It is also highly compressible, making it a strong acoustic scatterer.

2.3 Subharmonic bubble response and the effect of ambient pressure

Understanding the subharmonic response of an UCA is a complex challenge. Depending on the type of bubble used, the acoustic pressure[919] and pulse frequency[1920 21] have to be carefully chosen. At high acoustic driving pressures, the contribution of the lipid shell and its stiffness becomes negligible, and the

resonance frequency of the bubble approaches that of a free gas bubble. Therefore, when investigating the effect of the composition of the bubble shell, it is important to use a low acoustic pressure (< 50 kPa[19]).

A lipid coated microbubble of radius r has a corresponding radial and shell dependent resonance frequency f_o. A cloud of microbubbles does not have a single resonance frequency, but a range of resonance frequencies, shaped like a bell curve. When the bubble cloud is monodisperse, this bell curve of resonance frequencies narrows down towards ideally a single resonance frequency. Driving the microbubble acoustically at this resonance frequency, the subharmonic is expected at half of the resonance frequency. This method is called TR (Transmit at $1 * f_0$, Receive at $\frac{1}{2} * f_0$). Chomas *et al.* showed that the TR subharmonic oscillations are predicted to occur when the transmission frequency is the same as the bubble resonance frequency. However, in optical experiments, it was found out that resonant-sized bubbles can become unstable while driving them at resonance frequency, even at low acoustic pressures. Sometimes the bubbles even broke down, resulting in a weak subharmonic response.

Chomas observed that during T2R (Transmit at $2 * f_0$, Receive at f_0), the bubbles would not be destroyed, while the subharmonic intensity would be higher. This is believed to be due to the fact that the frequency at which the subharmonic response is observed is the actual resonance frequency of the bubble. Also, the threshold excitation pressure (the minimal acoustic pressure from which point a subharmonic component can be measured) is lower for T2R than for TR[19][20].[21] Simulations also confirm this, as seen in Figure 7. Here, the mean subharmonic power is shown, normalized with the fundamental. For T2R, as the acoustic pressure increases, the scattered mean subharmonic signal rapidly increases. The same happens for TR, but with lower scattered power. According to simulations, at high acoustic pressure TR starts to overtake T2R, but in reality bubbles don't survive high acoustic pressures at TR.

The shell elasticity (Equation 4) also plays an important role in the presence of a subharmonic response. It has been shown that a rapid change in shell elasticity in combination with a small change in surface area generates subharmonics of high intensity[19].[22] Since the shell elasticity is the derivative of the interfacial surface tension curves in Figure 6, the second-order derivative of these curves is thought to be the driving factor behind the generation of subharmonics.

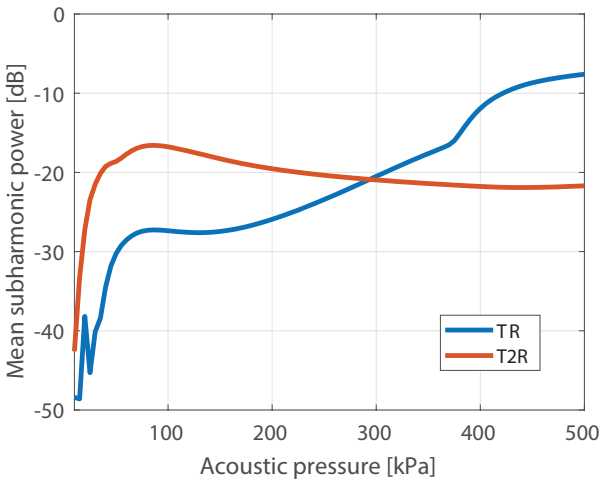

Figure 7: **Simulations of TR vs T2R subharmonic response**. 45% PA, f = 3.4 MHz for T2R, f = 1.7 MHz for TR. The threshold acoustic pressure at which T2R starts to increase is lower than that of TR. The increase of T2R is also bigger than the increase of TR.

.

Whenever the change in slope of the surface tension curves from Figure 6 is the highest, the T2R subharmonic response is expected to be maximal. In the Marmottant model, there are two points where the change in slope of the surface tension is maximum: At the transition points from the buckled to elastic domain and the elastic to ruptured domain.

As explained in the section on bubble modelling, the ambient pressure affects the radius of the bubble. Increasing the ambient pressure causes the bubble radius to decrease. This in turn decreases the surface area of the bubble, causing the ratio of surface area $\frac{A}{A_0}$ to decrease. This corresponds with a decrease in surface tension with respect to the initial surface tension (Figure 8). For every arbitrary surface tension, oscillations of the acoustic pressure of the pulse cause extra oscillations around this surface tension as well.

When gradually increasing the ambient pressure, the surface tension will gradually go down, until the bubble reaches the buckled state. Since the surface tension is decreasing towards the point where the change in gradient of the surface tension is maximum, theoretically the subharmonic bubble response will increase as the bubble approaches the buckled state. At some arbitrary ambient overpressure, the point of maximum change in slope near the transition point from elastic to buckled is reached. Around this point, the intensity of the subharmonic response is expected to be at its maximum.

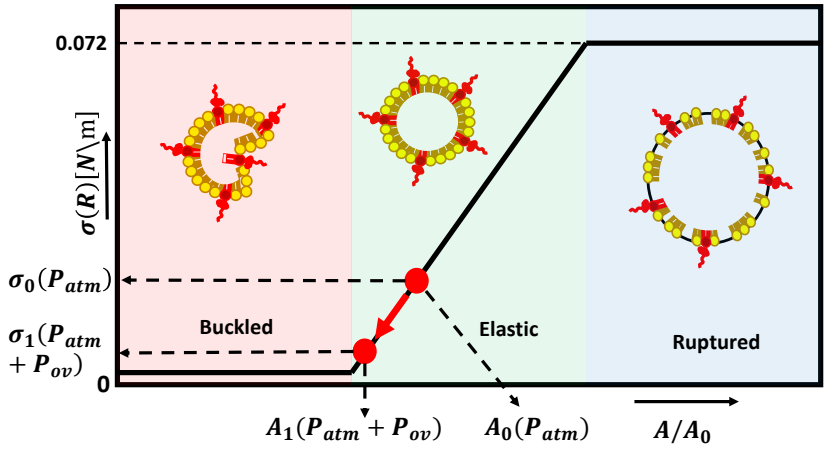

Figure 8: **The effect of ambient pressure on the Marmottant model.** Increasing the ambient atmospheric from P_{atm} to $P_{atm} + P_{ov}$ decreases the surface area ratio $\frac{A}{A_0}$, which in turn decreases the surface tension.

3 Materials and methods

In this chapter, the materials and methods used in experiments, data analysis and simulations are discussed. The experiments conducted in this thesis consist of three parts: Bubble synthesis, bubble characterization and changing ambient pressure measurements performed with the bubbles. First, the synthesis of the bubbles is discussed. This consists of which lipids are chosen, how they were prepared for use in the bubble maker and how the bubble maker makes the bubbles. Secondly, the bubbles are characterized. This includes performing Coulter measurements to determine the bubble size and monodispersity, as well as acoustical characterization of the bubbles to check if they are viable for performing T2R measurements. After that, the Verasonics system, as well as the setup and procedures and data processing steps followed to perform and analyse the experiments are discussed. Finally, the simulations performed to gain a better understanding of the results are explained.

3.1 Bubble fabrication

3.1.1 Lipids

The lipids used are DSPC and DPPE-PEG5000, both purchased at Corden-Pharma. The palmitic acid, a small amphiphilic fatty acid, has a $\geq 99\%$ purity and is purchased from Sigma-Aldrich. The lipid mixture was prepared by dissolving a $9:1$ molar ratio of DSPC and DPEE-PEG5000 in a solvent mixture of $2:1$ volume ratio of chloroform ($\geq 99\%$ pure) and pure methanol ($\geq 99\%$ pure). The dissolving in the solvent mixture ensures an even mixing and dissolution of both the lipids in the final solution. If the final goal was to make X mL lipid mixture, the lipids should be dissolved in 1.2X solvent mixture. The concentration of the lipids was 12.5 mg per mL of the X mL lipid mixture. To this, a variable mol% of palmitic acid could be added. Examples of amounts of lipids and palmitic acid are shown in table 1. After the lipids and the palmitic acid were dissolved, the mixture was transferred to a spinning Rotavapor flask, which was placed in a pre-heated 65° C water bath. After this, a vacuum was carefully applied to evaporate all the solvents, leaving behind a thin film of mixed lipids on the inside of the flask. This vacuum was left for at least 2 hours, preferably more, to completely ensure all solvents were evaporated.

After carefully lifting the vacuum, the required X mL amount of isoton dilutant was added to the flask. This flask was then left rotating in the heated water bath to ensure all lipids dissolved into the isoton, for at least 15 minutes. In order for the palmitic acid to dissolve into the isoton, the water bath temperature had to be above 63° C. Finally, the lipids dissolved in isoton were transferred into a plastic container and placed in the refrigerator. Here, they could last for an extended period of time, until use in the bubble maker.

X [mL]	% PA [mol%]	DSPC [mg]	DPPE-PEG [mg]	PA [mg]
30	0	207	167	0
30	30	207	167	32
30	45	207	167	61

Table 1: Amount of lipids and palmitic acid (PA) used to create certain mol% PA lipid mixtures. By increasing the amount of PA while keeping amount of the DSPC and DPPE-PEG5000 constant, the mol% PA can be increased. All the lipids and PA in the table above were dissolved in 25 mL chloroform and 12.5 mL methanol

3.1.2 Bubble maker

The bubbles used in the experiments were synthesized in the bubble maker. The bubble maker utilizes a flow-focusing microchip in combination with three mass flow controllers (MFC's), a pressure controller, lipids and gas to create microbubbles. A schematic view of the bubble maker setup is displayed in Figure 9. All the components are contained in an insulating PVC casing, which is kept at 67 °C by an electronic heater in combination with a fan to ensure homogeneous heating. The setup is kept at such high temperatures to ensure minimal coalescence of the bubbles.[23] If temperatures drop below the threshold of 63°C, lipids can coalesce together, which can cause bubble coalescence, resulting in lower monodispersity. The MFC's, pressure controller, pressure sensors and a camera are connected to an external PC. On this PC, a MATLAB script is run which lets the user read data from the pressure sensors located in the bubble maker, as well as control the flows through the MFC's and corresponding flow-focusing microchip channels.

In the bubble maker, the lipid solution is injected into a tank and are pressurized by C_4F_{10} gas. This lipid tank leads to a Bronkhorst LIQUI-FLOW^{TM} liquid mass flow controller (MFC 3 in Figure 9), which directly connects to the flow focusing microchip. Through a different tube, the same C_4F_{10} gas flows to a Bronkhorst EL-FLOW Select F-200CV MFC (MFC 2 in Figure 9). This gas flows into a buffer, located before the pressure controller, where it mixes with CO_2 gas that is controlled by a Bronkhorst EL-FLOW Select F-200DV MFC (MFC 1 in Figure 9). In this buffer, a mixture of 80% vol:20% vol $CO_2 : C_4F_{10}$ is maintained. The mixture of a low- and high-acqueous solubility gas ensures a monodisperse and highly stable, non foaming microbubble suspension.[24]

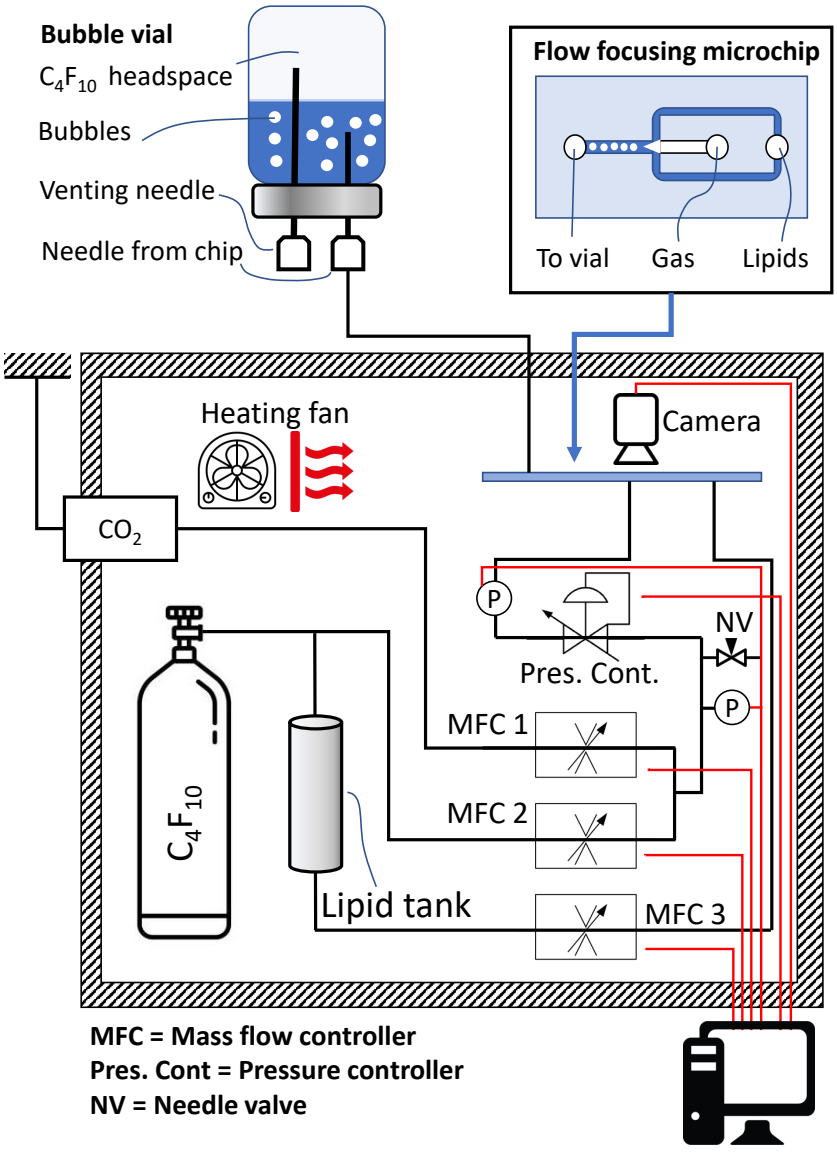

Figure 9: **Schematic view of the bubble maker.** Multiple components, all connected to a host computer, ensure control over parameters that affect the bubble creation inside the flow focusing microchip.

The gas mixture flows to the flow focusing microchip, while the pressure on the mixture is regulated by a Bronkhorst EL-PRES P-602CV pressure controller, which forms a feedback loop with two pressure sensors in order to ensure a controlled gas flow to the microchip. A needle valve is used to prevent over-

pressure on the pressure controller. Both the gas and the lipids are connected to the microchip using Peek microfluidic tubing. In the flow focusing microchip, the flows of the lipids and the gas mixture meets in such a way that a gas jet is formed, creating monodisperse microbubbles (see Figure 10). The size of the microbubbles can be controlled by altering the gas pressure of the gas mixture and the flow rate of the lipids. Bubble production rates of up to 10^6 bubbles per second can be reached.[14]

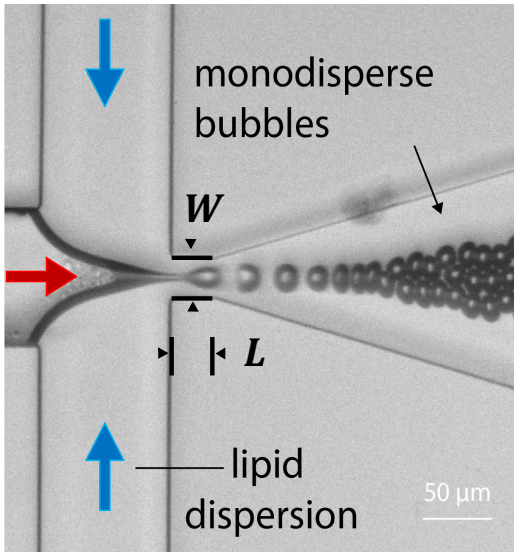

Figure 10: **Close-up of the flow-focusing device.** C_4F_{10} and CO_2 gas mixture (red arrow) flows towards the exit channel, where it is squeezed by two perpendicular flows of lipid dispersion (blue arrows). The bubbles are created in a channel of width W = 21 µm, length L = 30 µm and a depth of 16 µm.

3.1.3 Bubble synthesis

Bubbles were created using the bubble maker. First, the interior of the bubble maker would be heated to 60° C. Due to this, the vapor pressure of the C_4F_{10} would increase, resulting in the ability to pressurize the lipid mixture and chip with gas. Also, high temperatures are needed to flush out any remaining lipids from previous sessions out of the tubes and controllers. This was done by injecting >50 mL of ultraclean MilliQ into the lipid tank and flushing it through the bubble maker using CO_2 gas. Before injecting the lipid mixture into the lipid tank, they were sonicated using a Branson 250 sonicator with a Model 102C(CE) tip for 3 sets of 90 seconds at a total amplitude power of 20%. This breaks up lipids that can have coalesced during storage and transportation. Sonication is complete when the lipid mixture turned from cloudy to clear.

After flushing and cleaning, a clean microfluidic chip was inserted in the bubble maker. After this, the C_4F_{10} gas tank was opened and the pressure in the buffer was set to 3.3 bar (at the location of the pressure controller below the needle valve in Figure 9. Next, the pressure on the microfluidic chip was set to 1.7 bar. In order to control the created bubble size, the flow rate of the lipids was varied (see Table 2 for example parameters).

Vial #	**Gas pressure [Bar]**	**Flow rate [mL/hr]**	**Diameter [µm]**
1	1.7	4	10
2	1.7	5	9.2
3	1.7	4.7	8.5
4	1.7	5	7.7
5	1.7	7	5.7
6	1.7	7.7	5.4
7	1.7	8.5	2.7
8	1.7	8.7	2.6

Table 2: **Example of used parameters and resulting bubble sizes.** Created 0% PA bubbles in a single session of bubble making together with used bubblemaker parameters. The bubble diameter was measured with the Coulter counter. Note that created bubble diameter does not directly scale with the flow rate of the bubble maker. Making two vials with the same flow rate can result in two differently sized bubbles.

Next, the bubbles are transported to a vial filled with C_4F_{10} to prevent diffusion of the gas in the bubbles to the surroundings, ensuring stabilization.[24] A small venting needle was used to ensure atmospheric pressure in the vial. Note that copying the settings from table 2 does not mean that bubbles with identical size will be created. There are many uncontrollable factors that affect the size and concentration of created bubbles, such as cleanliness of the microfluidic chip, tubes, pipes and state of the controllers and temperature of the chip.

3.2 Bubble characterization

Before using the bubbles in the ambient pressure setup, it is important to partly characterize the bubbles. In this case, it means determining the bubble radius and the bubble resonance frequency. Knowing the bubble resonance frequency is required in order to know at which frequency the bubbles should be excited, and if T2R is possible with the probe. In this subsection, the use of the Coulter counter and the attenuation setup is explained.

3.2.1 Bubble sizing

The bubble size distributions were measured using a Beckman Multisizer 3 Coulter Counter. This Coulter counter utilizes an aperture in glass tube submerged in isoton. A cathode applies a voltage across the isoton, while an anode inside the machine measures the voltage. Whenever a particle flows through the aperture, the voltage applied on the isoton and glass tube changes. From this voltage change the Coulter counter can then determine the size of the particle that went through the aperture. After a few seconds of flow through the aperture, an accurate histogram containing the bubble distribution is obtained.

For every measurement, 50 µL of bubbles were diluted into 100 mL of isoton. After letting the bubbles stabilize for 2 minutes, three runs per vial of bubbles were performed, with a waiting time of 60 seconds in between. Upon dilution, excess C_4F_{10} gas diffuses out of the bubble until a stable size is reached.[24] For all the bubbles used (0%, 30% and 45% PA), this process was observed to take 2-3 minutes by looking at histograms taken at different times after dissolution. The averages of the second and third Coulter measurements (after stabilization) are plotted in Figure 11. The mean bubble radii are 2.87 µm for 0% PA, 3.23 µm for 30% PA and 3.05 µm for 45% PA. The monodispersity was expressed with the polydispersity index (PDI), which is defined as the division of the mean by the standard deviation:

$$\text{PDI} = \frac{\sigma}{< r >} \cdot 100\%. \tag{11}$$

Ideally, this method is only used for perfect gaussian distributions. Bubble distributions can be skewed, but Figure 11 shows that the measured curves are not significantly skewed, and thus Equation 11 can be used. This resulted in a PDI of 10% for 0% PA bubbles, 9% for 30% PA bubbles and 11% for 45% PA bubbles (See Table 3). The cumulative concentration of all bubbles was around $300{\cdot}10^6$ bubbles per milliliter.

mol% PA	**0**	**30**	**45**
Mean radius [um]	2.87	3.23	3.05
Standard deviation [um]	0.104	0.091	0.115
PDI [%]	10	9	11

Table 3: **Mean radius, standard deviation and polydispersity index of the bubbles** All bubbles have an about equal polydispersity index.

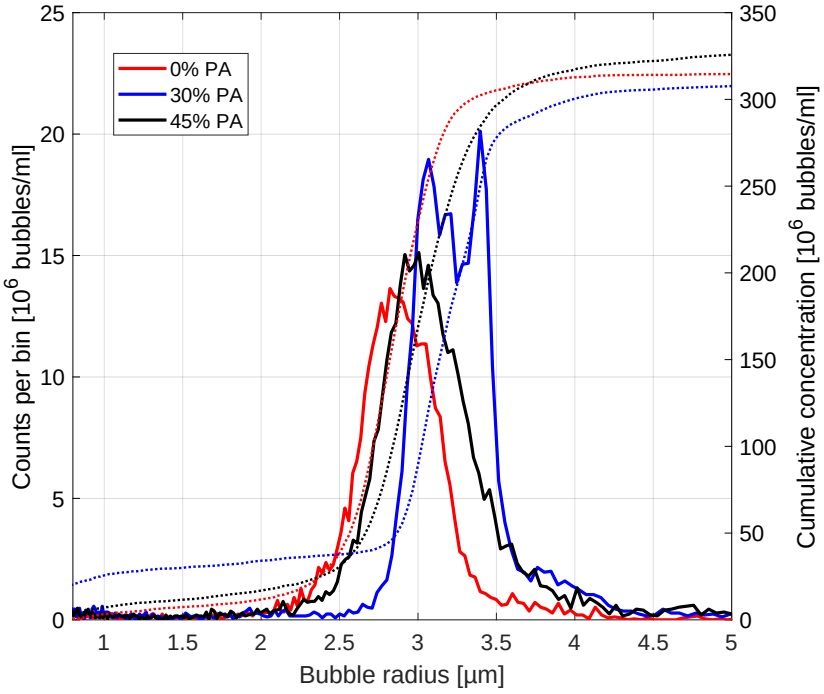

Figure 11: **Coulter measurements of the used bubbles.** The mean radii are 2.87 µm for 0% PA, 3.23 µm for 30% PA and 3.05µm for 45% PA, with a polydispersity index of 9, 10 and 11% respectively. Total concentration of all three bubbles is around $300{\cdot}10^6$ bubbles per milliliter.

3.2.2 Attenuation setup

The attenuation setup is used to determine the resonance frequency of the bubbles. The attenuation setup transmits an ultrasound pulse that travels through the bubble cloud, after which the remaining signal is measured with another ultrasound transducer. The frequency at which the original signal has attenuated the most is the resonance frequency. The setup is displayed in Figure 12.

On a host computer, the user can determine which pulses have to be transmited through the bubble cloud. The host computer sends the pulse information to a TABOR 8026 Arbitrary waveform generator. This pulse information can consist of combinations of pulses with many frequencies and transmit voltages. The host computer is also connected to a Berkeley Nucleonics Corp (BNC) model 575 Digital Delay / Pulse generator. This BNC triggers both the waveform generator as well as a Picotech PicoScope 5000 series. When triggered, the waveform generator transmits the pulses to a Vectawave VBA100-200 Amplifier, which amplifies the pulse signal and sends them to a Olympus V304,

1.88” focal length transmitting transducer. The transmitting transducer then transmits the pulses through a bubble container placed in a large bath of water.

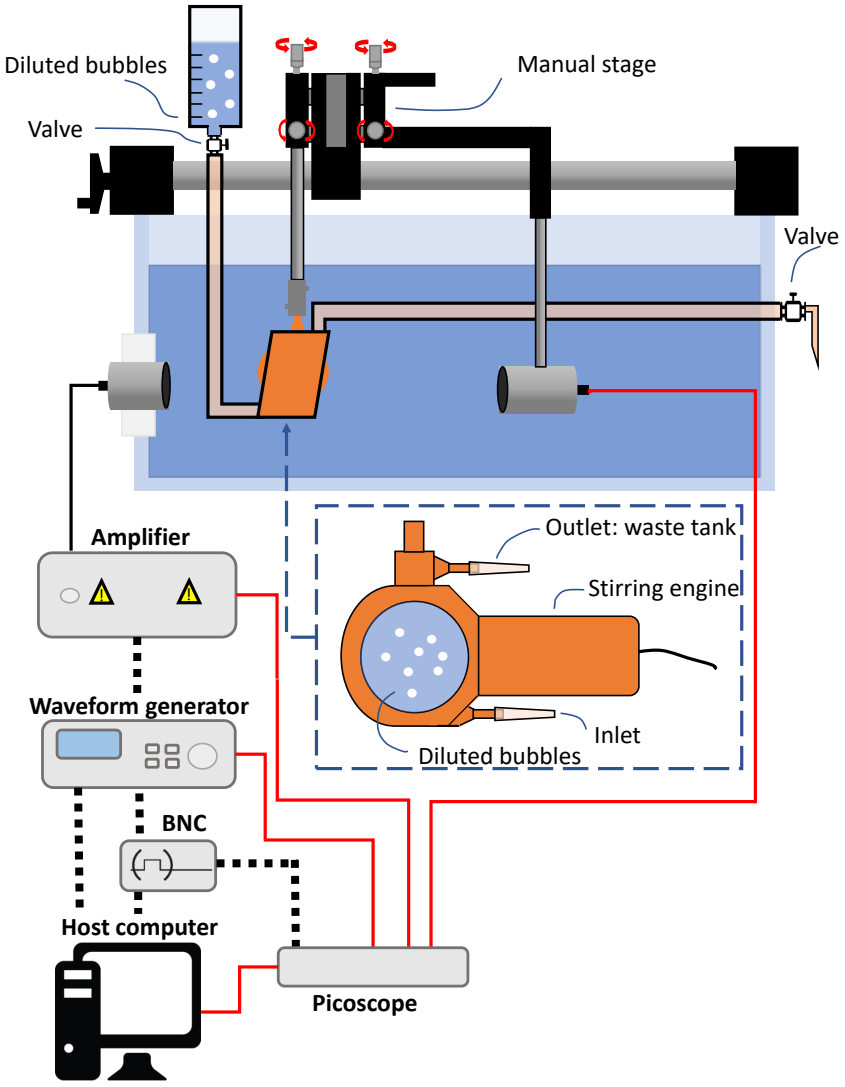

Figure 12: **Schematic view of the attenuation setup**. The bubble container was submerged in a water tank, in which a transmitting and receiving transducer were located. A host computer connected to multiple hardware components controlled and measured the transmitted and received pulses.

This bubble container consists of a bubble chamber that has two ports: An inlet through which freshly diluted bubbles can be introduced, and an outlet

which is connected to the waste tank. A magnetic stirring engine is connected to the bubble container. This magnetic stirring engine rotates quickly, causing a small spherical magnet in the bubble chamber to rotate, which ensures a homogeneous bubble cloud throughout the chamber at all times. While the pulses travel through the bubble cloud, the individual bubbles absorb energy, causing the pulse to attenuate. Behind the bubble container, a receiving transducer (Olympys V307, 1.94" focal length) that is aligned with the transmitting transducer is placed. The receiving transducer is coupled to the picoscope, which transfers the data of the waveform generator, transmitting transducer and the receiving transducer to the host computer.

Next, the host computer utilizes a MATLAB script to analyse the obtained transducer data into attenuation curves of the bubbles. In order to calculate the attenuation of the bubbles, two receive transducer measurements are compared: One reference measurement, in which the bubble container is filled with just isoton, and one measurement in which the container is filled with the bubble solution. The frequency spectrum of both measurements is determined, after which the attenuation is calculated by dividing the maximum amplitude of the reference measurement by the maximum amplitude of the bubble measurement. Finally, the data is transformed into the dB scale:

$$\text{Attenuation [dB]} = 20 \cdot log_{10}\Big(\frac{\max(\text{reference measurement})}{\max(\text{bubble measurement})}\Big). \tag{12}$$

When this is done for a range of transmit frequencies, the attenuation of the bubbles for all these frequencies can be determined. Plotting the results gives the attenuation spectra of the bubbles for many different acoustic pressures.

3.2.3 Attenuation measurements

The water tank was filled with demineralized water. Before performing attenuation measurements, the setup first had to be calibrated. First, the receiving transducer was aligned with the transmitting transducer by placing the receiving transducer in the focus of the transmitting transducer. This was done by adjusting the position of the receiving transducer until the voltage signal of the receiving transducer was maximized. After this, the receiving transducer was moved back into the far field of the pulse, while the bubble container was inserted into the focus of the beam. Careful alignment is crucial for comparing measurements from different days. Extra care was given to removing air bubbles sticking to the bubble container or surfaces of the transducers.

Measurements were performed by sweeping over the frequency and the acoustic pressure of the pulse. The frequency vector was 05:0.1:5 MHz while the pressure vector was 7.5:7.5:100 kPa. For every acoustic pressure, all frequencies were repeated three times for averaging.

First, the setup was flushed with isoton in order to ensure that no more old bubbles remained in the container. Then, a reference measurement of the container containing isoton was taken. After this, between 1 to 20 µL of bubbles, depending on which concentration was required, was diluted into 100 mL of isoton. After giving the bubbles three minutes to stabilize in the solution, the setup was flushed and filled with the solution. Next, the bubble measurement was performed, after which the setup was flushed twice, once with demineralized water and once with isoton. A secondary reference measurement was taken after each bubble measurement, to ensure reference measurements for every bubble measurement. The attenuation spectra of the used bubbles are shown in Figure 13.

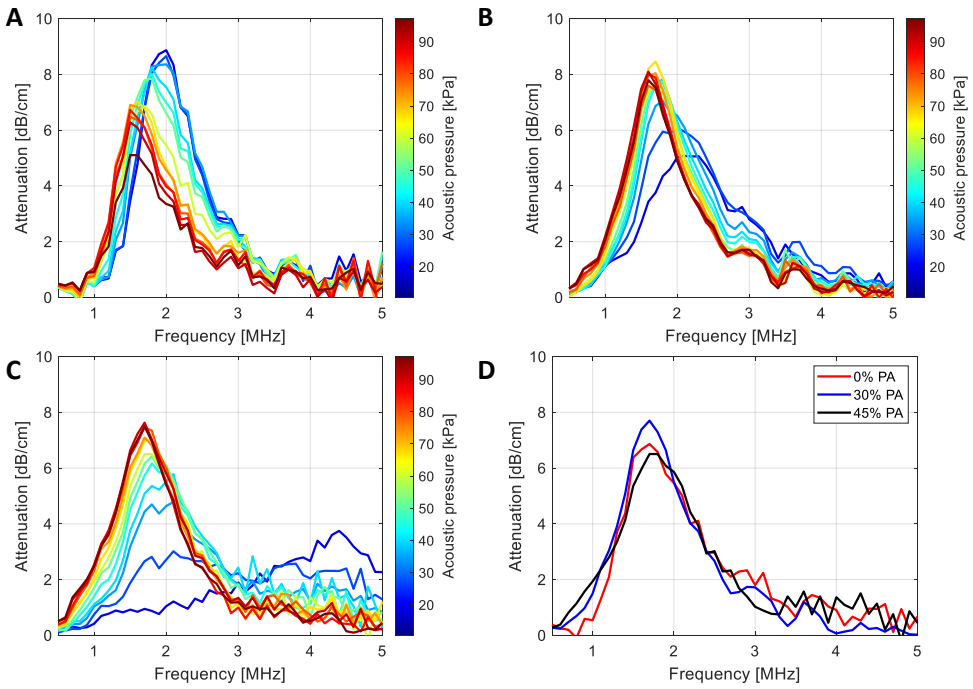

Figure 13: **Attenuation measurements of the used bubbles at a concentration of 22.500 b/ml. A:** 0% PA at a range of acoustic pressures, **B:** 30% PA at a range of acoustic pressures, **C:** 45% PA at a range of acoustic pressures, D: 0%, 30% and 45% PA at an acoustic pressure of 50 kPa. While the bubbles have different radii, the bubbles resonate at the same frequency for the higher acoustic pressures.

While the bubbles have different sizes, they resonate at the same frequency for acoustic pressures above 30 kPa. The resonance frequency is inversely dependent on the radius of the bubbles: a large bubble has a lower resonance frequency than a small bubble. Since the 30% and 45% palmitic acid bubbles

are larger than the 0 palmitic acid bubbles, a lower resonance frequency is to be expected. However, Figure 13 shows that the resonance frequency is equal for all bubbles, which implies that palmitic acid increases the resonance frequency of the bubbles. This was also predicted by Equation 10.

The effect of the palmitic acid is also seen at low acoustic pressures. For all bubbles, at lower acoustic pressures the resonance frequency starts to shift towards higher frequencies. For 0% PA (Figure 13 A, this shift converges to 2 MHz, while for 45% PA the shift converges to 4.5MHz. These values can be used to calculate the each bubble's shell elasticity. The elasticity of the bubbles was extracted from Figure 13 with the following Equation, derived from Equation 10:

$$\chi = \frac{R_0}{4}\Big(\rho R_0^2(2\pi f_0)^2 - 3\kappa P_0 - (3\kappa - 1)\frac{2\sigma(R_0)}{R_0}\Big), \tag{13}$$

where R_0 is the mean radius of the bubbles, ρ is the density of water (1000 kg m^{-3},f_0 the resonant frequency at the lowest acoustic pressure, $\kappa = 1.07$ the adiabatic polytropic exponent, P_0 the atmospheric pressure (100 kPa) and $\sigma(R_0)$ the initial surface tension (40 Nm^{-1}). This results in an elasticity of 0.57 Nm^{-1} for the 0% PA bubbles, 1.4 Nm^{-1} for the 30% PA bubbles and 4.9 Nm^{-1} for the 45% PA bubbles (See Table 4). This is perfectly in line with the results presented at EchoContrast 2021 (Figure 5 B). However, it is unexpected that the 30% PA bubbles have a larger radius than the 45% PA bubbles, but an equal resonance frequency. Equation 13 shows that stiffer bubbles are expected to be larger in order to have the same resonance frequency than less stiffer bubbles. From this, the 45% PA bubbles are expected to be larger than the 30% PA bubbles, but this is not the case, and it is unclear why.

mol% PA	**0**	**30**	**45**
Resonance frequency at low acoustic pressure	1.9	2.2	4.5
Stiffness χ [N/m]	0.57	1.4	4.9

Table 4: **Bubble shell stiffness values found with equation 13.**

3.3 Verasonics system

To investigate the effect of increasing the ambient pressure on the nonlinear bubble response for different kinds of bubbles, A Verasonics Vantage 256 System was used. The Vantage research ultrasound platform offers a combination of hardware and software in order to provide direct access to raw ultrasound data, while preserving the ability to perform real-time imaging at clinically relevant frame rates. The software can be combined with custom MATLAB scripts which allow the user control over ultrasound pulse parameters, measurement region and data transfer. The hardware of the Vantage 256 system is shown in Figure 14.

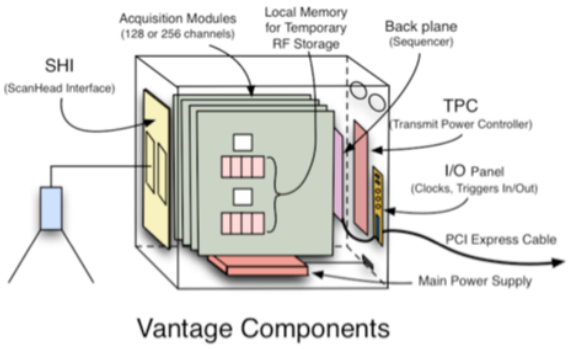

Figure 14: **Vantage 256 System unit hardware components**. The hardware unit consists of several components to which the ultrasound probe, host computer and triggers can be connected.

The scanhead interface is the hardware module that contains the transducer connectors. The Vantage 256 system contains a dual connector supporting up to 256 channels. These connectors offer to possibility to connect ultrasound probes that are used in clinical settings. This gives the advantage over single element transducers that research performed with the system can more easily be related to a clinical setting. The scanhead interface is connected to the acquisition modules, where the circuitry for transmitting and receiving ultrasound signals is located. The scanhead interface samples at a rate of 250 MHz. Each acquisition module supports up to 64 transmitting and receiving channels. In the acquisition modules, ultrasound signals are digitized and stored in local memory. In this digitalization, the signal sampled at 250 MHz is decimated to 42.67 MHz. This sampling rate is more than enough to sample the wanted frequencies (1.7 and 3.4 MHz). The back plane module contains the hardware sequencer that controls the operation of the acquisition modules. This back plane module is connected to an external host computer with the PCI express cable. On this host computer, the acquisition scripts are selected and run in MATLAB. After a measurement, the data is transferred from the acquisition modules to the host computer. The Vantage 256 also contains an Input/Output panel, on which a Trigger In and Trigger Out is located. The trigger out maintains a constant voltage of 3.5V, but while a trigger is activated this drops to 0V for a few microseconds. This trigger is used to activate the ambient pressure sensor.

For the scattering experiments, an ATL P4-1 Phased Array Transducer was used. In clinical settings, this transducer is used in order to image the cardiac region of patients. The P4-1's bandwidth reaches from 1 to 4 MHz, and is centered around 2.5 MHz. The transmit, receive and two-way transfer functions are shown in Figure 15. The transmit and receive transfer functions show small amounts of amplitude response loss around the center frequency of the transducer. Below 1.5 MHz and above 3.4 MHz a rapid decrease in amplitude

response is observed. In order to investigate T2R-subharmonics, a driving frequency twice that of the resonance frequency of the bubbles is needed. Also, it is advantageous for both the driving frequency and the frequency at which subharmonics will be emitted to have the same amplitude response. Between 1.7 MHz and 3.4 MHz, there is only an amplitude response difference of 0.4 dB, while the amplitude response decrease with respect to the center frequency is only 3.5 dB. For this reason, a driving pulse of 3.4 MHz is used, which means subharmonics are expected to occur at 1.7 MHz.

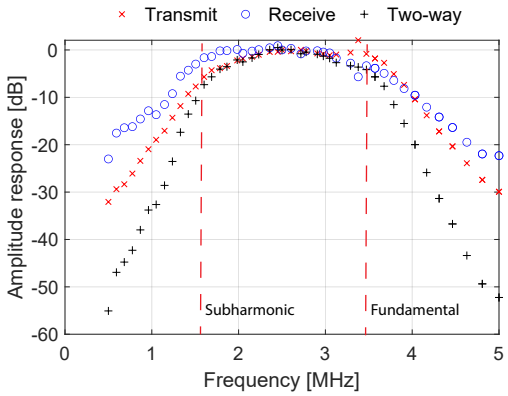

Figure 15: **Transfer functions of the P4-1 probe.** The transmit (red), receive (blue) and two-way (black) all three show small amounts of amplitude response loss around the center frequency of 2.5 MHz. Red dashed lines indicate the transmitted frequency (fundamental), and the frequency at which the subharmonic will be measured. Transfer functions measured by Nathan Blanken.

3.3.1 Beam and pulse

The beam that is used during the experiments is focused on a point 20 cm away from the probe interface. The bubble container will be located 3.5 cm away from the probe interface. This difference focal distance and container distance means that the ultrasound pulse can be approximated as a plane wave as it hits the container. Lateral and elevational cross-sections of the pulse are shown in Figure 16. These figures were obtained with a transmit voltage of 2.5 V and measuring the resulting field with a calibrated hydrophone. The red squares in the figure display the location of where the bubble container will be during experiments. At 2.5 V, the average acoustic pressure in the red square would be 60 kPa. The acoustic pressure scales linearly with the voltage, so at 5 V the average acoustic pressure in the red square would be 120 kPa. The minimum voltage of the Vantage 256 is 1.6 V, which translates to a minimal acoustic pressure of 40 kPa.

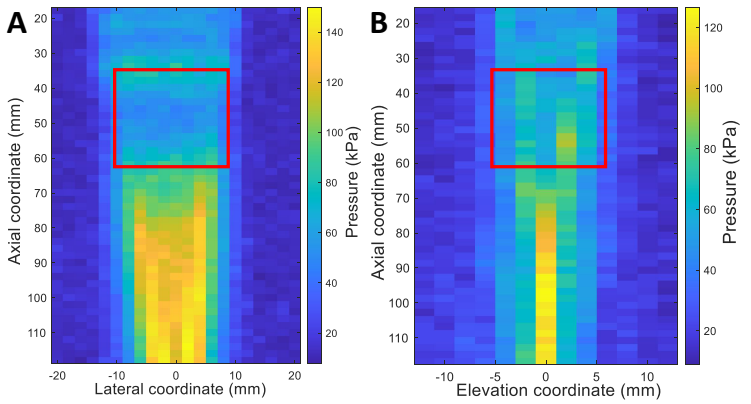

Figure 16: **Cross-sections of the used beam transmitted at a transducer voltage of 2.5V with the P4-1 probe.** Obtained using a calibrated hydrophone by Nathan Blanken and Benjamin van Elburg. **A:** Lateral cross-section. **B:** Elevation cross-section. The red rectangle indicates the position of the bubble container during bubble scattering experiments.

The shape of the pulse, reflected from a metal plate, is shown in Figure 17. The pulse has a length of 16 cycles and its frequency is 3.4 MHz. A pulse length of 16 cycles was used because from preliminary tests resulted that this pulse length resulted in limited reflections from the front and back window, while also resulting in the ability to measure subharmonics. If the number of cycles is lowered, there are less reflections of the container, but also less time for the bubbles to scatter signal, lowering the scattered subharmonic signal substantially. In order to maintain a constant amplitude of the pulse, it is only tapered around the first half and last half cycle.

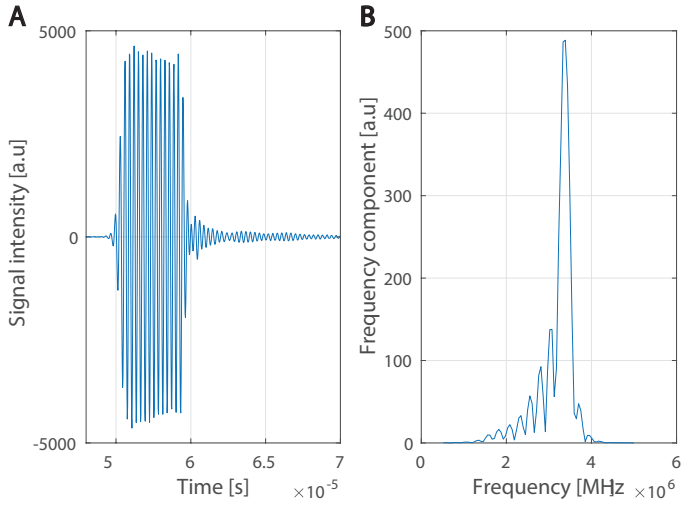

Figure 17: **Metal-plate reflection of 3.4 MHz pulse. A:** Reflected pulse. This reflection is not an exact copy but a good visualization of the pulse that the bubbles experience. **B:** Fourier transform of the reflection of the pulse. The dominant frequency in the spectrum is 3.4 MHz.

3.3.2 Ambient pressure setup

The ambient pressure setup (Figure 18) combines the same water tank used in the attenuation setup (Figure 12) with the Verasonics Vantage 256 system to perform scattering measurements on the bubble container. To the container, a combination of components that enables the hydrostatic pressure in the container to be increased in a controlled matter is connected.

Whenever a measurement is started by activating the script on the Verasonics host computer, the P4-1 starts making 1000 acquisitions (Transmit and Receive), with 7.5 µs between each acquisition. In total, this makes the duration of a single measurment 7.5 seconds. After the first 10 acquisitions, the Vantage hardware unit is programmed to trigger the BNC. The BNC then responds by sending a continuous trigger to the Picoscope, to which the pressure sensor is connected. The Picoscope then starts saving the voltage of the pressure sensor from 2 seconds before the trigger to 8 seconds after the trigger at a sampling rate of 10kHz. This voltage can then be converted to a hydrostatic pressure by using a conversion factor. Once the trigger is activated, the syringe pump has to be manually activated in order to compress the air in the system and therefore increase the hydrostatic pressure. Since the lengthy duration of a single measurement, there is enough time to increase the pressure.

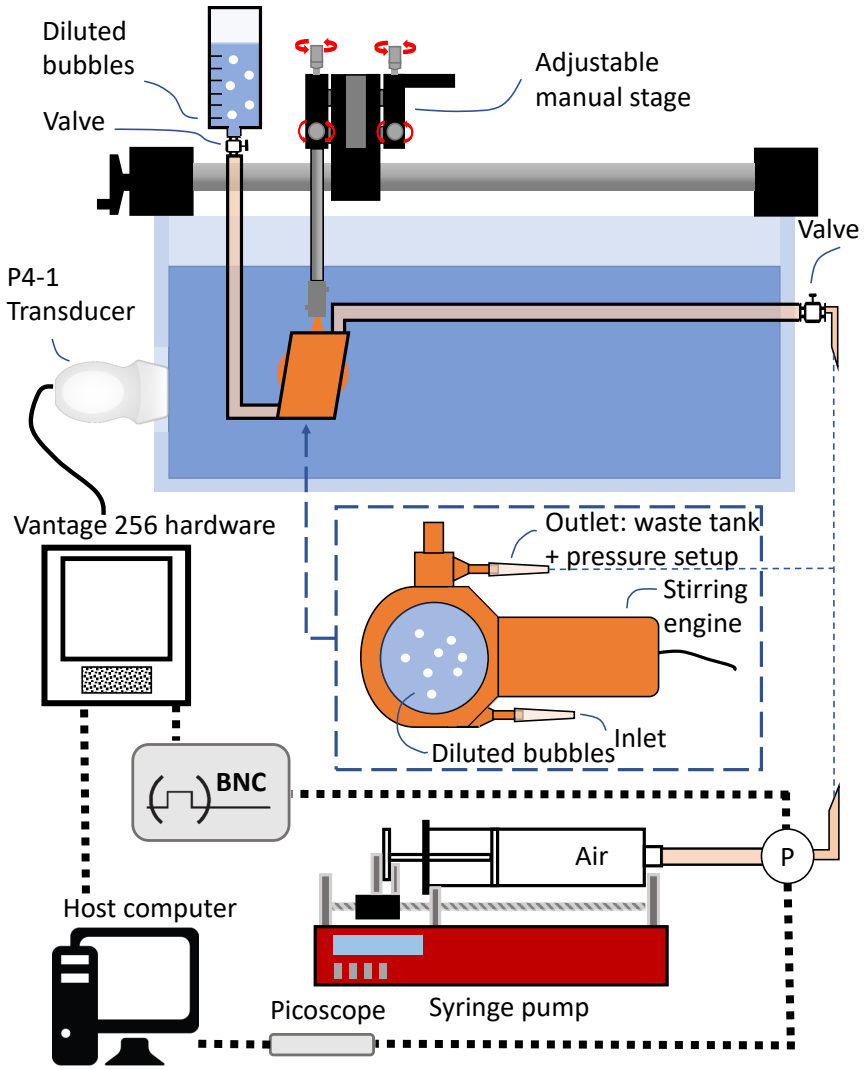

Figure 18: **Vantage 256 System unit hardware components**. The same water tank as in the Attenuation setup is used, with a larger bubble container.

To increase the ambient pressure inside the container continuously, a syringe pump is connected to the outlet of the bubble container. Valves at the inlet and to the waste tank of the system can be closed, causing the system to be closed off. Now, the airtight syringe pump can be used to increase the hydrostatic pressure in the system in a continuous way. In between the syringe pump and the bubble container, a pressure sensor that constantly monitors the ambient pressure in the closed off system, is located. A

typical curve of the pressure inside the container is shown in Figure 19.

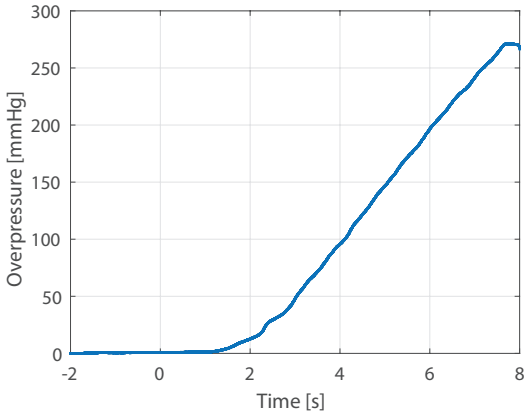

Figure 19: **A typical pressure curve of the experiments.** After a brief unstable increase, the hydrostatic pressure starts to increase linearly. After 7.5 seconds, the measurement is done, and the pressure can be decreased.

3.3.3 Changing ambient pressure measurements

For the changing ambient pressure measurements, the hole for single element transducers in the water tank was closed off using thin cling film taped to the inside of the tank. Once again, the water tank was filled with demineralized water and the bubble container was screwed into place. The P4-1 probe was placed in a clamp and pushed onto the cling film with acoustic gel in between. The probe was orientated horizontally such that the lateral section of the pulse (Figure 16 A) was parallel to the surface of the water in the tank.

Before performing a measurement, the entire setup was flushed with demineralized water and isoton consecutively. After this, 1 to 20 µL of bubbles, depending on the required concentration, was diluted into 100 mL of isoton. After three minutes of stabilization, this solution was then used to flush and fill the bubble container. Next, the valve leading to the waste tank and the valve controlling the flow into the system were closed, resulting in the system being closed off. Next, the Verasonics script was activated, which started the measurement. After a short time the trigger would be observed on the host computer, which resulted into manually activating the syringe pump. After the measurement was done, the syringe pump had to be manually turned off. After a measurement, the data was saved on the host computer and the setup was prepared for the next measurement by depressurizing, flushing the bubble container with demineralized water and isoton, after which a new bubble solution was diluted and put into the system. If there were enough bubbles, measure-

ments were repeated at least three times for each concentration and acoustic pressure.

3.3.4 Data processing

In a short period of time, the Verasonics collects large amounts of data. This is processed into readable data using MATLAB. In this subsection, the steps taken to go from raw data to dB intensity graphs are explained.

First, data has to be selected such that only bubble signal is analysed. Essentially, the Verasonics captures 96 individual RF signals. By ordering the elements and plotting all the 96 RF signals in a single plot, an extremely basic 'image' showing the times of occurring reflections can be made. This is seen in Figure 20, where A) displays the RF signal of the container without the presence of bubbles, while B) displays the RF signal of the container while it is filled with bubbles. A clear difference between just the isoton and the bubbles diluted in isoton is observed.

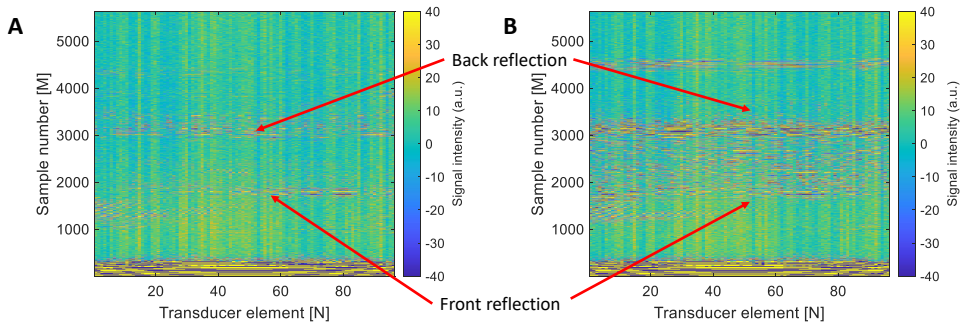

Figure 20: **Full RF signal of the 96 elements in the P4-1 probe measured while scanning a container. A:** Filled with isoton. **B:** Filled with diluted bubbles. In (A), the front and back reflections of the container are clearly visible. The isoton between the two reflections does not scatter, while in (B) the bubble solution in the container does scatter the transmitted pulse.

Only the RF data belonging to the time window containing the bubble signal is selected. In order to minimize signal losses due to attenuation, data is selected from the front reflection of the container to just before the back reflection of the container. This window is visualized with a red square in Figure 21. Two different types of windows are chosen: One containing all the bubble signal in one single window, and one containing all the bubble signal in six different sections, giving the ability to analyze the bubble signal as a function of depth in the container. Attenuation changes the amplitude of the acoustic pressure transmitted by the transducer. By dividing the bubble signal into smaller sections, the attenuation for each section can be calculated, which enables an

acoustic pressure estimation per section.

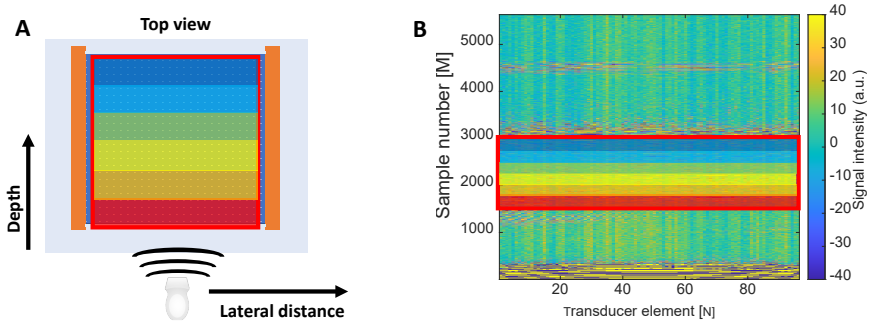

Figure 21: **Data selection window visualized. A:** A top view cross section of the container. **B:** The full RF signal of all 96 elements. Colored sections represent the windows that were selected for the over depth analysis of the container.

The next step is determining the powerspectra of each section. This is done by calculating the fast fourier transform (fft) of each individual RF signal with the appropriate window. Then, these are all summed together and divided by the total number N of RF signals:

$$F(f) = \frac{1}{N} \sum_{n=1}^{N} \frac{|\text{fft}(\text{RF}(N,t))|}{L}, \tag{14}$$

where fft(RF(N,t)) is MATLAB's fast fourier transform of the measured RF signal for element N and time window t. The length of the time window can be changed in order to accommodate the entire container or the different depth sections of it. The data is then transformed to the dB scale, where it was normalized by the fundamental power at ambient pressure of the second depth section:

$$\text{Power [dB]} = 20 \cdot \log_{10}\left(\frac{F}{F_{\text{fund,2,ambient}}}\right) \tag{15}$$

The second depth section was used over the first depth section since it does not contain any reflections of the front window. In order to determine the bandwidth of the frequencies belonging to both the fundamental and subharmonic receive frequency, a fourier transform of the transmitted pulse was taken. The distance between the two minima closest to the transmit frequency is chosen to be the bandwidth of chosen frequencies for the analysis (Figure 22). The value of Δf is 0.233 MHz.

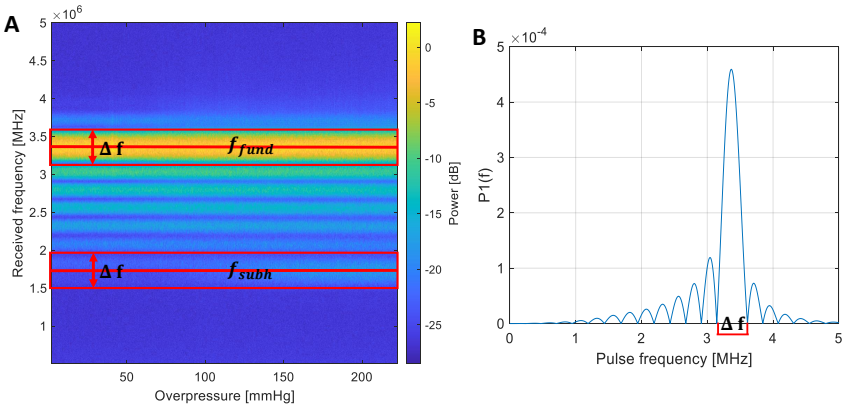

Figure 22: **Selecting the bandwidth of frequencies belonging to the fundamental and subharmonic response. A:** Complete measurement of received frequency versus overpressure for 45% PA bubbles. The transmit frequency is 3.4 MHz, so the subharmonic will occur at 1.7 MHz. The red regions display regions of the fundamental and subharmonic frequency, with bandwidth Δf. **B:** Zero-padded fourier transform of transmit pulse. The bandwidth Δf is determined by the distance between the two minima close to the transmit frequency of 3.4 MHz (displayed in red).

To find the intensity of the fundamental, for every of the 1000 acquisitions, the average value between 3.4 $\pm\frac{0.233}{2}$ MHz is taken. For the intensity of the subharmonic, the same is done for 1.7 $\pm\frac{0.233}{2}$ MHz. The time at which every acquisition is made is known, so it can be coupled to a measured ambient pressure. The power spectra are then binned into bins of a width of 3.75 mmHg: all power spectra of acquisitions made between 0 and 3.75 mmHg are placed in bin 1, all power spectra of acquisitions made between 3.75 and 7.5 mmHg are placed in bin 2 and so on, until all power spectra are placed in a bin. The number of acquisitions in a single bin is sufficiently high such simple internal statistics accurately represent the data sets. The mean of all the values in a single bin is saved as the measured acoustic response for that pressure range, while the standard deviation within a single bin is seen as the statistical internal error. Figure 23 shows the individual datapoints of each acquisition, as well as the binned means with standard deviation as error region.

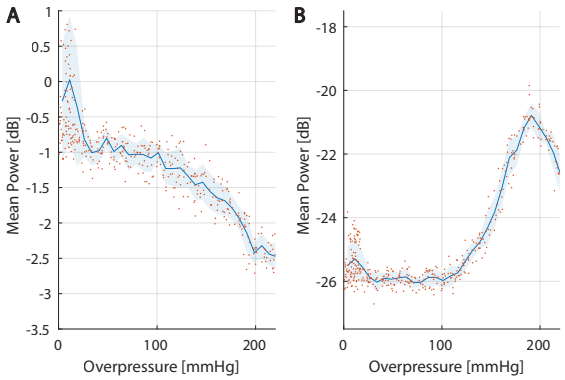

Figure 23: **Plots containing both data points of individual acquisitions (orange) as well as binned means with standard deviation represented by the blue shaded area. A:** Fundamental mean power. **B:** Subharmonic mean power. Both the binned fundamental and subharmonic mean power with error bars shows to be a good visualization of the data.

In the same script, the acoustic pressure corresponding to the 6 different depth sections and time windows is also calculated, using the method described by Segers *et al.*[25] This is done by using the time of the RF signals to calculate the depth at which the bubble container is located in the water tank. This depth is then used to select the relevant region of the entire pulse (an example pulse at 2.5 V in Figure 25 A & B). The relevant area of the pulse is then divided into the same 6 sections that are used in the power spectrum analysis, and the mean of these sections is taken (Figure 25 C). The final step in calculating the acoustic pressure of the individual sections is implementing the attenuation of the bubbles. Attenuation measurements are made to obtain frequency and acoustic pressure dependent attenuation values for the bubbles at all bubble concentrations. By making the assumption that the acoustic pressure is constant over each of the 6 sections, an average attenuation over every individual section can be made. The decrease of acoustic pressure due to attenuation is then calculated from the front to the back of the container. First, the attenuation on the first depth section is calculated. The ratio of the acoustic pressure after divided by the acoustic pressure before the attenuation is then used to apply attenuation on the second depth section. This results in a new initial acoustic pressure for the second depth section, which will also be attenuated by the bubbles within that section. A new ratio of acoustic pressure from before and after is calculated to determine a new initial acoustic pressure in the third depth section, and so on (Figure 24).

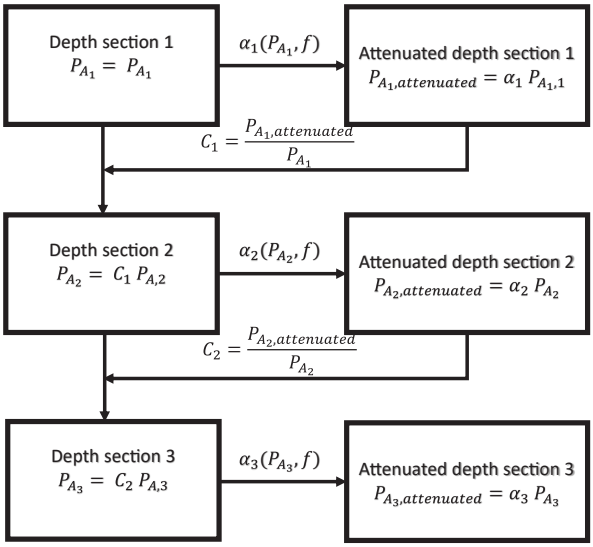

Figure 24: **Block diagram showing how attenuation due to bubbles is calculated.** Every depth section is affected by the attenuation of previous depth sections, as well as the average attenuation occurring in its own section.

This is done for all 6 sections, with every section that is deeper into the container being affected by previous sections as well. The result are displayed in Figure 25 D, where attenuation of 45% PA bubbles at a concentration of 60.000 bubbles per milliliter results in a 40% decrease in acoustic pressure for the final section.

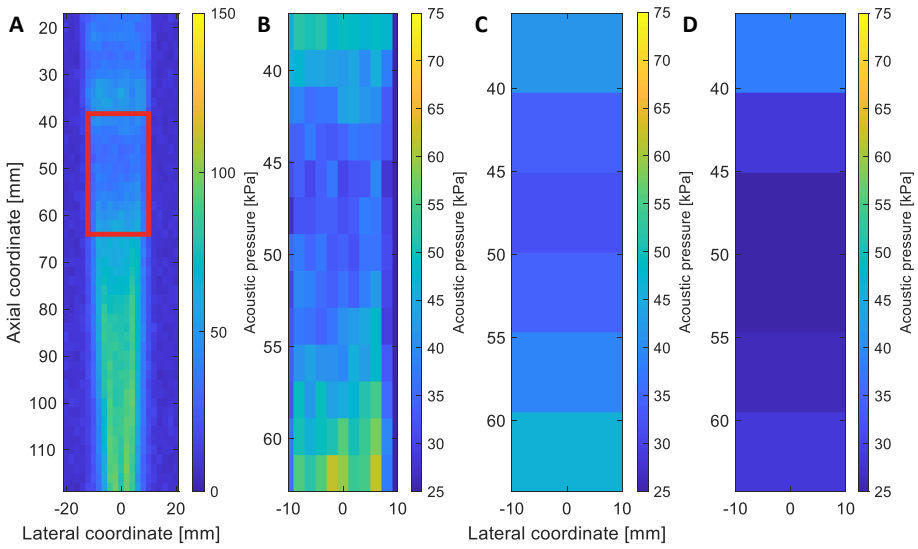

Figure 25: **Acoustic pressure inside the bubble container. A:** Lateral cross section of the entire pulse. Red rectangle shows the area where the bubble container is. **B:** Part of the lateral cross section that is located inside the bubble container (red rectangle in A). **C:** Six depth parts, where the acoustic pressure was determined by averaging the values belonging to each depth part from B. **D:** Final acoustic pressure over depth including bubble attenuation caused by 45% PA bubbles at a concentration of 60.000 bubbles per milliliter.

In order to compare the subharmonic scattering performance of the different bubbles and concentrations, the variable called the corrected change of subharmonic (CCoS) is introduced. The CCoS is the increase of the subharmonic response with respect to the fundamental. For every overpressure, the corresponding fundamental is subtracted from the corresponding subharmonic response. This is then normalized with the fundamental minus the subharmonic response at atmospheric pressure:

$$\begin{aligned} \text{CCoS(P1)} = &\Big(\text{Mean Power}_{\text{fund}}(\text{P1}) - \text{Mean Power}_{\text{subh}}(\text{P1})\Big) - \\ &\Big(\text{Mean Power}_{\text{fund}}(0) - \text{Mean Power}_{\text{subh}}(0)\Big) \end{aligned} \tag{16}$$

This means that the CCoS is zero for atmospheric pressure, while it is nonzero for other overpressures while the fundamental and subharmonic change at a different rate. The CCoS is illustrated in Figure 26, where an increase of the CCoS is shown after the ambient pressure starts to increase. The maximum value of the CCoS (7.7 dB in Figure 26 B) is used in order to compare the performance of different concentrations and depth sections in the container. The purpose of the CCoS is to see if it is possible to determine the blood pressure

in a human body, therefore it is not necessary to evaluate the CCoS above an overpressure of 200 mmHg.

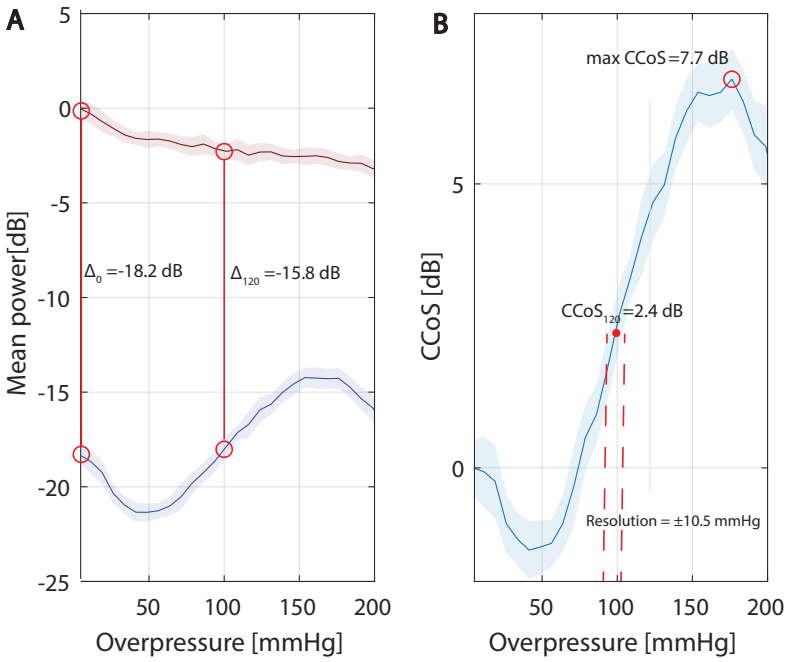

Figure 26: **Calculating the corrected change of subharmonic (CCoS) A:** Example measurement of a fundamental (red) and subharmonic (blue) bubble response. The difference between the fundamental and subharmonic at ambient pressure is -18.2 dB, while it is -15.8 dB at an overpressure of 100 mmHg. **B:** Plot of the corrected change in subharmonic. The CCoS is determined by looking at the increase or decrease with respect to the difference between the fundamental and subharmonic response at ambient pressure. At the overpressure of 100 mmHg, this is -15.8 - -18.2 = 2.4 dB. The maximum CCoS is 7.7 dB, at an overpressure of 175 mmHg.

It is important to note that an increase in CCoS is not only determined by the increase of the subharmonic, but can also be caused by a decrease of the fundamental. If, in any case, the subharmonic stays constant but the fundamental drops by a significant amount, the CCoS will increase by the same amount. It is therefore important to keep in mind the fundamental and subharmonic behavior individually as well. Resolution is defined as the width of the errorbars, and is also displayed in Figure 26. Whenever a certain dB level gets measured, the CCoS can belong to that range of overpressures.

3.4 Bubble simulator

Equation 1 was solved in MATLAB in order to aid the understanding of the measured data. These simulations can then be employed to understand the mechanisms that influence the CCoS. The simulator is written by Nathan Blanken, who gave permission to use and edit it. In the simulations, the surface tension was based on the Marmottant model described in the set of equations 3. The model takes into account the physical properties of a lipid monolayer shell formed around a gaseous microbubble. The effect of the increasing ambient pressure on the bubble size, surface tension and gas density was determined using the description given in equation 9. In the simulations, material properties were the density $\rho = 998$ kg m^{-3}, atmospheric pressure $P_0 = 101.3$ kPa, speed of sound $c = 1500$ m/s, polytropic coefficient $\kappa = 1.07$, liquid viscosity $\mu = 0.001$ Pa·s. The initial surface tension was chosen as a variable that can be changed in order to fit simulations to measured data, and ranged between 10 and 70 mN/m. κ_s and damping constants are calculated dynamically within the simulator.[1626] χ and R_0 were chosen as the same values found in the bubble characterization section. Furthermore, the acoustic pressure and frequency were set at $P_A = 40$ kPa, $f = 3.4$ MHz, with a length of 16 cycles. However, when necessary, the simulator can also sweep over a range of acoustic pressures and frequencies.

The simulator solves equation 3 with an ordinary differential equation solver (MATLAB ode45). For a given value of ambient pressure, acoustic pressure, frequency and initial surface tension, the corresponding radial bubble response (R,$\dot{R}$) and new equation parameters (damping coefficients,polytropic exponent) are obtained.

4 Results

In this chapter, the results of the ambient pressure measurements, as well as simulations of the fundamental and subharmonic microbubble responses are shown. First, the effect of both the depth and bubble concentration in the container on the bubble signal will be discussed. Based on these results, the depth from which the different molar fraction palmitic acid bubbles are compared is selected, once all for the same depth, and once for the depth at which yielded the best CCoS for each individual bubble type. In the next section, a comparison of the CCoS between the different molar fraction palmitic acid bubbles at these depths is made. In the following section, the resolution of the ambient pressure detection based on the CCoS is calculated and compared with the clinically required resolution. In the final section, simulations of single bubbles are used to gain a better understanding of the important parameters concerning the fundamental and subharmonic response, as well as the CCoS. Whenever the bubbles are described with a molar fraction PA, the results are experimental, while when the bubbles are described with the stiffness χ, the results are from simulations. When depth of a section is discussed, the average depth of that section is used to simplify the results.

4.1 The effect of depth and concentration on the bubble signal

In this section, the effect of specific depth and concentration on the acoustic pressure field inside the container, and scattered signal will be shown. Figure 27 shows the acoustic pressure inside the container, calculated with the method described in Figure 25, as well as the maximum CCoS for every concentration and depth section of 0% PA (A and D), 30% PA (C and E) and 45% PA (E and F) bubbles.

Figures 27 A, B and C show the acoustic pressure in the bubble container with the 0%, 30% and 45% PA bubbles respectively. In all the calculated pressure maps the original pressure field from Figure 25 C is displayed: The pulse pressure decreases as the depth increases, but at the end of the container the pulse pressure increases again. This is most pronounced for the low concentrations, where the pressure field follows the original pressure field from Figure 25 closely. At higher concentrations, the attenuation increases, and outweighs the increase in pressure due to the focusing of the beam. The attenuation spectra of the bubbles (Figure 13) differ the most at their resonance frequencies. Since the bubbles are driven at twice their resonance frequency, at pressures above 20 kPa, the attenuation of the three different bubbles is very similar. This results in a similar trend for all acoustic pressure maps: the acoustic pressure increases with bubble concentration and depth. For low concentrations, the acoustic pressure at the end of the container increases slightly because of low attenuation and a converging pulse pressure field. Figures 27 D, E and F show the maximum value of the CCoS in the bubble container for the 0%, 30% and 45% PA bubbles

respectively. Here, the maximum CCoS is displayed, irrespective of its location.

For all types of bubbles, the acoustic pressure inside the container decreases as depth and concentration increases. For low concentrations, the calculated pressure maps follow the pressure field from Figure 25 C. The CCoS of 0% bubbles decreases for higher concentrations, while for 30% and 45% PA bubbles the maximum CCoS increases for higher concentrations. The CCoS of PA bubbles perform best at the lowest acoustic pressures.

Figure 27 D shows the maximum CCoS for the 0% PA (χ = 0.57 N/m) bubbles. It shows that after the first depth section (at 4.28 mm), the CCoS decreases dramatically. This is almost certainly caused by attenuation of the scattered subharmonic signal. The pressure scattered by the microbubbles has a very low acoustic pressure in comparison with the acoustic pressure of the transmitted pulse. Figure 13 A shows that, for low acoustic pressures, the peaks of the attenuation curves converge to 2 MHz. Since bubbles attenuate a lot at frequencies close to the resonance frequency, there is a significant amount of attenuation at the frequency at which the subharmonic is measured (1.7 MHz). This is also the reason why the highest value of CCoS is seen at the concentration of 7500 bubbles per milliliter, in the first depth section, since attenuation is still low. In the case of 0% PA bubbles, this concentration seems to balance an increase in bubble signal with an increase in attenuation.

Figure 27 E shows the maximum CCoS for the 30% PA (χ = 1.4 N/m) bubbles. This figure differs a lot from Figure 27 D, since in the case of the 30% PA bubbles an increase in maximum CCoS for increasing depth and concentration is observed. Figure 13 B shows that, for low acoustic pressures, the attenuation at 1.7 MHz decreases significantly because of the increased stiffness, see Equation 10. This means that the subharmonic signal that is scattered from the stiffer bubbles does not attenuate as much as the 0% PA bubbles. The highest maximum CCoS is observed at the highest concentrations and deepest parts of the bubble container. These places correlate with the places where the acoustic pressure is minimum. It is known that the effect of adding palmitic acid (i.e. increasing bubble stiffness) is best seen at lower acoustic pressures[18][19] . At higher acoustic pressures, the radial excursion becomes large enough for the elastic region of the bubbles to be less significant. The maximum CCoS for 30% PA is highest at a concentration of 30.000 bubbles per milliliter at the final depth section (17.96 mm).

Figure 27 F shows the maximum CCoS of the 45% PA (χ = 4.9 N/m) bubbles. The highest maximum CCoS value is measured at a concentration of 60.000 bubbles per milliliter, at the third depth section (7.7 mm) from the front window. In figure 27 C it shows that this concentration and depth correlates with the lowest acoustic pressure inside the container.

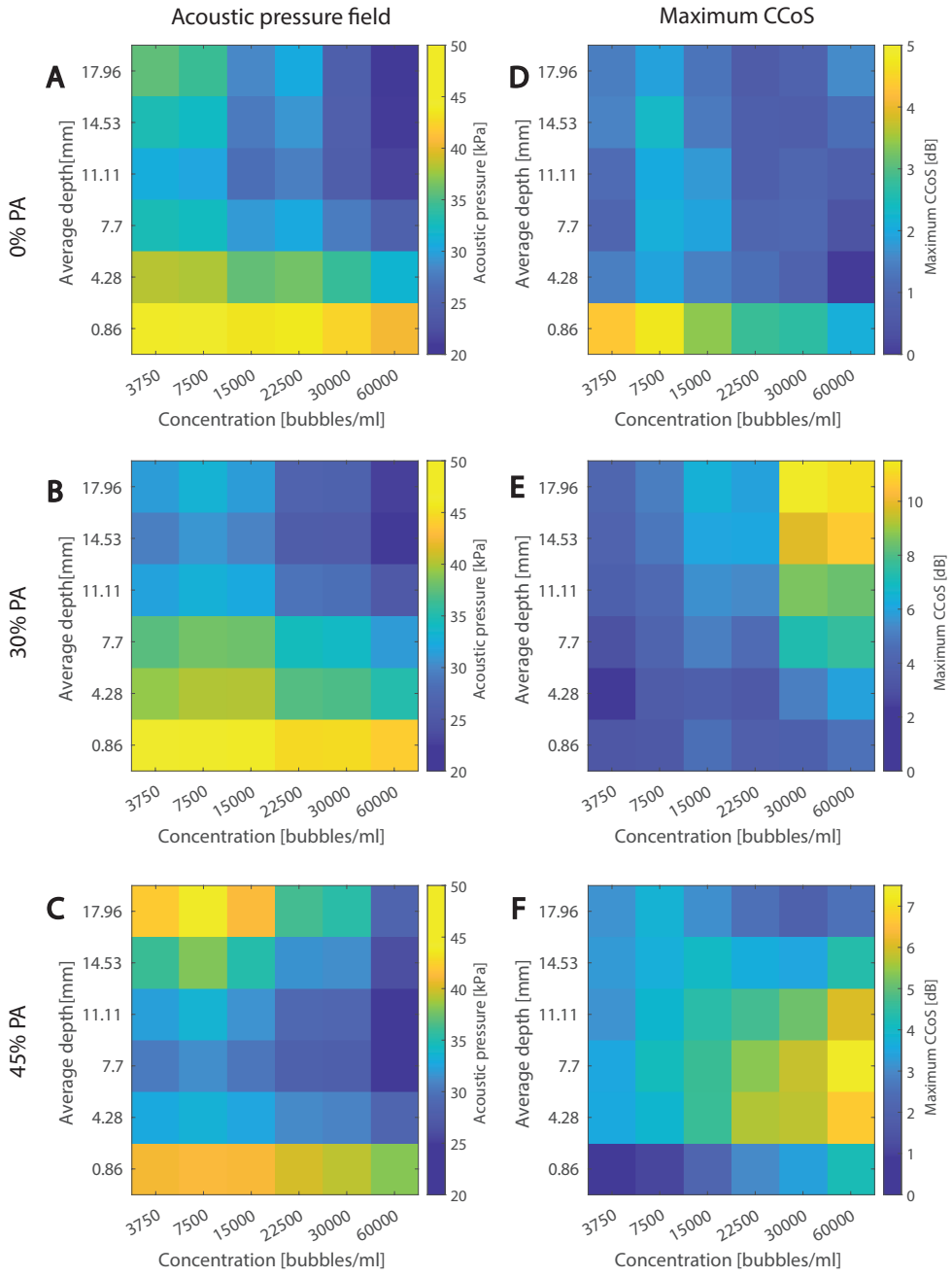

Figure 27: **Acoustic pressure and maximum CCoS as function of concentration and depth for 0%, 30% and 45% bubbles. A, B,C** Acoustic pressure inside the container for the 0%, 30% and 45% PA bubbles respectively. **D,E,F:** Maximum CCoS of the 0%, 30% and 45% PA bubbles respectively. Note the different colorbar limits for D, E and F.

At the location and concentration where the CCoS is highest for the 30% PA and 45% PA bubbles, both the fundamental and subharmonic have an effect on the CCoS. Figure 28 shows an example of the 30% PA bubbles at a concentration of 30.000 bubbles/ml with the highest CCoS of 11.8, with both the fundamental and subharmonic response, as well as the CCoS. Figure 28 A shows that, as overpressure increases, the fundamental mean power only slightly decreases. The maximum CCoS value of 6.4 dB is mainly due to the increase of the subharmonic. At the final depth section, just before the back window, the fundamental changes a lot due to the influence of overpressure (Figure 28 C). This results in a maximum CCoS value of almost twice that of the second depth section (Figure 28 D). Here, the value of the maximum CCoS is influenced by both an increase in the subharmonic and a substantional decrease in the fundamental. From the current data, it is unknown what causes the behavior of the fundamental at greater depth and high bubble concentrations. Simulations later on in the chapter also do not predict this behavior. It only occurs for the palmitic acid bubbles, at high concentrations at the deepest sections of the bubble container, matching the locations of lowest acoustic pressures.

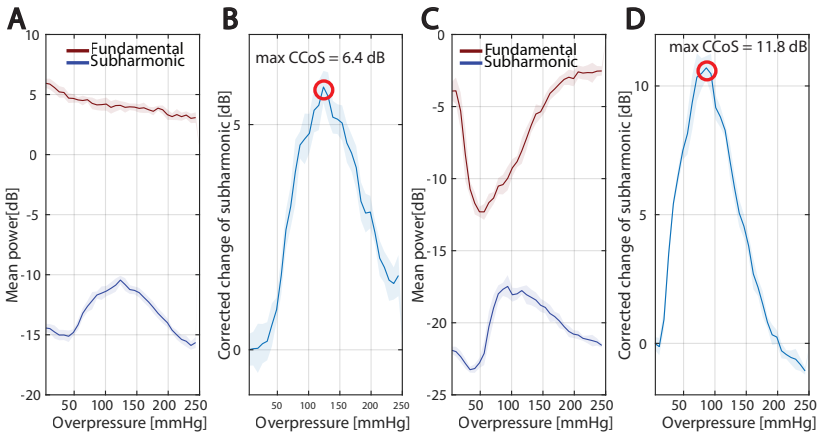

Figure 28: **Fundamental, subharmonic and CCoS graphs of the 30% PA bubbles at a concentration of 30.000 bubbles/ml, for the second and final depth section of Figure 27.** Normalized with the CCoS at atmospheric pressure. **A:** Fundamental and subharmonic of the second depth section (4.28 mm). **B:** CCoS of the second depth section. **C:** Fundamental and subharmonic of the final depth section. Notice the strong decrease followed by an increase of the fundamental as the overpressure increases. **D:** CCoS of the final depth section. Since the CCoS is also affected by behavior of the fundamental, CCoS increases a lot.

4.2 The effect of PA on the CCoS

In this section of the results, the CCoS of the three bubble types is compared. To quantitatively compare the results, the same depth section is used for all bubbles. This limits the complicating effects of attenuation. Figure 29 shows the CCoS of all bubbles and concentration for the second depth section. Here, the acoustic pressure for all sections is almost equal. The plots in the figure show that in all cases, the CCoS of the palmitic acid bubbles is higher than the CCoS of the 0% palmitic acid bubbles. As concentration increases, a gradual increase of CCoS of the 30 and 45% PA bubbles is observed, while for the 0% PA bubbles a decrease in CCoS is observed. This is due to attenuation of the scattered subharmonic, which lowers its measured mean power. The concentration of 22.500 bubbles/ml seems to be an outlier for this, as in the overpressure window the CCoS starts to increase where for other concentrations it does not. A possible explanation for this can be that the experiment with this concentration was performed before all other concentrations, which could have affected the initial surface tension by a different stabilization time or other accidental deviation from the experimental procedure. However, the overpressures at which this increase reaches a maximum is outside the range of a human's blood pressure, and are therefore irrelevant. The CCoS of the 30% and 45% palmitic bubbles both increase in the relevant range of overpressures (60-200 mmHg). Also, the increase of the CCoS looks similar, with the 45% PA's CCoS reaching only a slightly higher amplitudes than the 30% PA's CCoS.

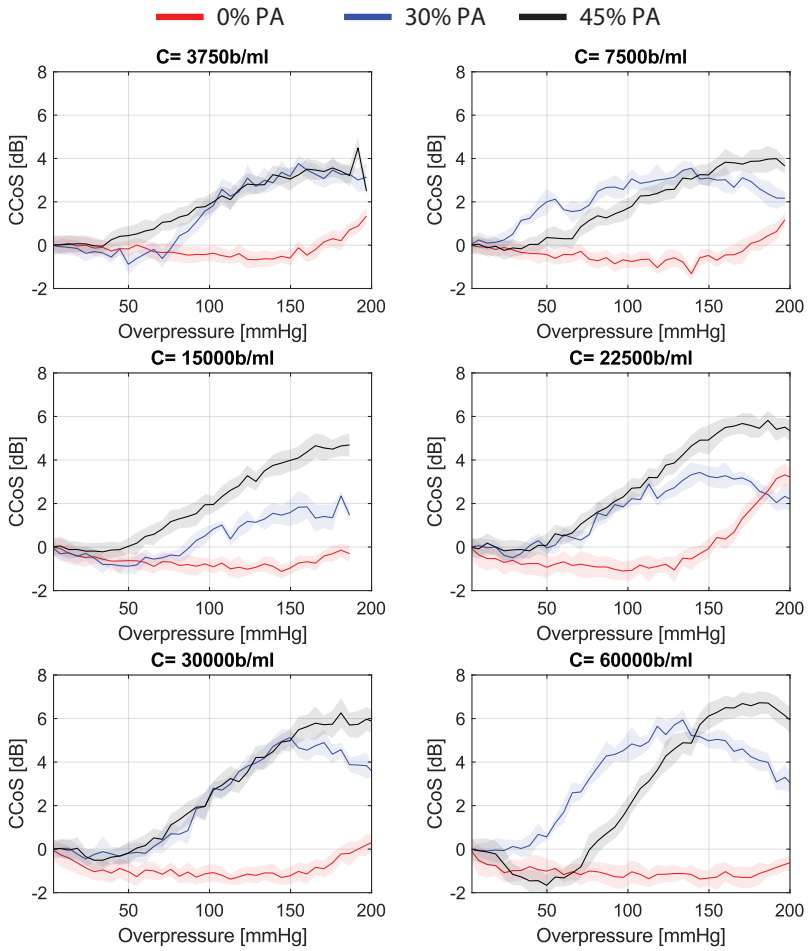

Figure 29: **CCoS of the three different bubble responses from the second depth section.** Concentration is displayed above the individual graphs.

Figure 30 shows the measurements containing the highest CCoS per bubble type. For 0% PA bubbles, this is the fourth depth section (11.11 mm) of 7.500 bubbles/ml, for 30% PA bubbles this is the final depth section at a concentration of 30.000 bubbles, and for 45% PA bubbles this is the final depth section at a concentration of 60.000 bubbles. Here, unexpectedly, the CCoS of the 30% PA bubbles is multiple dB above that of the 45% bubbles. This is not caused by a strong subharmonic response, but due to a strong fundamental decrease (Figure 28). High concentrations work well for the 30% and 45% PA bubbles, since the transmitted acoustic pressure, as well as the scattered subharmonic pressure are barely attenuated. Figure 13 shows that for low acoustic pressures

30% and especially 45% PA bubbles have low attenuation values for the subharmonic frequencies, while for 0% PA bubbles the attenuation values around the subharmonic frequencies is high.

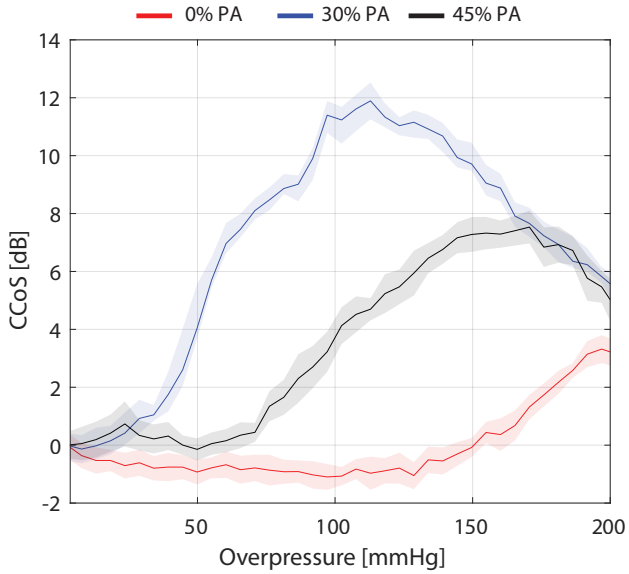

Figure 30: **Highest value CCoS curves.** Curves of the highest CCoS value found for every bubble type. 0% PA: $C = 7.500$ bubbles/ml, fourth depth section (11.11 mm). 30% PA: $C = 30.000$ bubbles/ml, final depth section (17.96 mm). 45% PA: $C = 60.000$ bubbles/ml, final depth section (17.96 mm).

Also, there is a difference in overpressure at which the CCoS occurs. This can also be seen in Figure 29, where the peak in the CCoS curves is reached for different overpressures for all kinds of bubbles. The overpressure at which the CCoS peaks is very important, since, for good ambient pressure estimations in the human body, it is relevant to have a substantial high-resolution increase or decrease in CCoS over the range of pressures inside the human body.

4.3 Resolution

A high resolution is essential for accurate and precise ambient pressure estimations. Resolution, here defined as the width of the error region at a certain measured dB level of the CCoS, should be below $\pm$ 2.5 mmHg in order to make accurate clinical assessments.[12] When the resolution increases to values above $\pm$2.5 mmHg, the margins are too high to make accurate assessments of a patients blood pressure and therefore alternative methods are still favored. A visual inspection of the error region in Figures 29 and 30 already shows that the error regions are wider than 10 mmHg, which means the resolution is in-

sufficient. The width of the error region is calculated for the regions where the CCoS increases, while the width of the error region for overpressures at which the CCoS remains constant are not taken into account. Pressure estimation will only be possible if the slope of the CCoS is high enough. The resolutions of the CCoS are shown in Table 5. For 0% PA, a resolution is not calculated since there is barely a slope in the CCoS, which results in resolutions of over 100 mmHg. The table shows that the value of the resolution is multiple times higher than the required resolution of ± 2.5 mmHg.

	0% PA	**30% PA**	**45% PA**
Mean resolution (Figure 29) [mmHg]	-	± 12.44	± 11.48
Resolution (Figure 30) [mmHg]	±13.37	±9.16	±9.68

Table 5: Mean resolution of the measurements shown in Figures 29 and 30. For clinical use, the resolution should be below ± 2.5 mmHg/dB. The results in the table show that the resolution of the experiments is multiple times worse than is required.

The size of the error region is most likely the effect of a changing local bubble concentration in the volume affected by the ultrasound pulse and the shape and tapering of the pulse. The bubbles in the bubble container are randomly distributed throughout the container, with a varying local concentration. This results in a differing amount of bubbles in the focus of the ultrasound pulse. This can, in turn, affect the amplitude of the measured signal. Also, not all bubbles have an equal initial surface tension, but the bubbles cover a range of initial surface tensions. This range in initial surface tension results in a spread of acoustic response as function of overpressure, increasing the width of the error regions as well.

4.4 Single-bubble simulations of the fundamental and subharmonic

In this section, results of the simulations of the acoustical response of the bubbles representing the experiments are shown. Values reported in the Materials and Methods (i.e. bubble radius, elasticity) are used as inputs of the Rayleigh-Plesset simulator. The transmit and receive frequencies are also the same in the experiments and the simulations. Since there are still a lot of differences between the experiments and simulations (bubble cloud vs single bubble, attenuation vs no attenuation, container vs no container, actual surface tension curves vs Marmottant), the simulations can not be used to replicate the measured results, but they can be employed to understand the mechanisms that influence the CCoS.

Figure 31 shows the simulated fundamental and subharmonic mean power of the three different bubble types as function of overpressure. Curves were normalized with respect of the fundamental mean power at atmospheric pressure. The initial surface tension is not well known and therefore has to be varied in

order to find a value of the surface tension that fits the results. This was done by checking the overpressure at which the mean subharmonic response peaks. A value of 40 mN/m was chosen in such a way that the overpressures at which the subharmonic peaks in the measurements matched that of the overpressures at which the subharmonic peaks in the simulations. In Figure31A, a decrease of fundamental mean power for all three bubbles is observed. As the molar fraction of palmitic acid increases, the fundamental mean power decreases as overpressure increases. This contributes to an increase of the CCoS. The $\chi = 4.9$ N/m bubbles show a small increase in fundamental at an overpressure of 150 mmHg, after which it decreases again. Figure 31B shows the subharmonic mean power for the different bubbles as function of overpressure. A substantial difference in both amplitude and location of the subharmonic peak is observed between the low stiffness ($\chi = 0.57$ N/m) and high stiffness ($\chi = 1.4$ & 4.9 N/m) bubbles. For the low stiffness bubbles, this peak occurs at a higher overpressure than for the high stiffness bubbles.

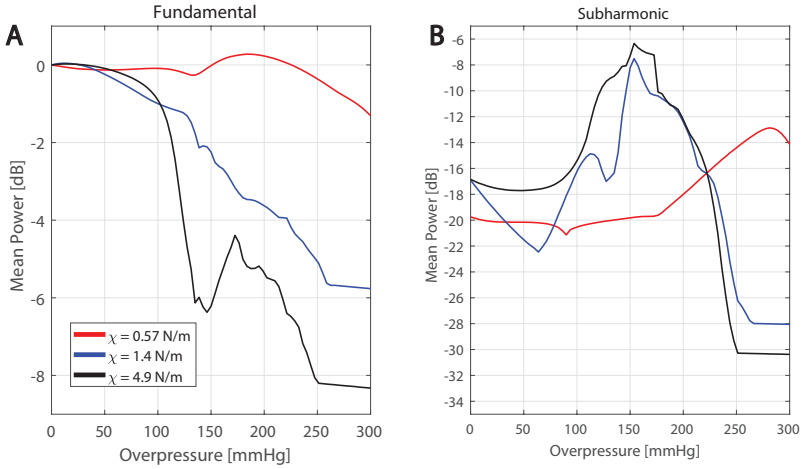

Figure 31: **Simulation of three bubble types with different stiffness, normalized with the fundamental at atmospheric pressure.** Marmottant model, other simulation parameters: $P_A = 40$ kPa, $f_D = 3.4$ MHz, $\sigma(R_0) = 40$ mN/m. **A:** Fundamental mean power of the three different bubbles. **B:** Subharmonic mean power.

Figure 32 shows simulations of the bubble radius normalized with the buckling radius of the individual bubbles, as well as the corresponding surface tension vales as function of overpressure. The buckling radius of the bubbles was calculated by rewriting Equation 3:

$$R_b = \frac{R_0}{\sqrt{1 + \frac{\sigma(R_0)}{\chi}}} \tag{17}$$

All peaks occur around the overpressure at which the surface tension hits zero, which indicates that the bubble is buckled. The stiffer bubbles ($\chi = 1.4$ N/m and $\chi = 4.9$ N/m) buckle at lower overpressures than the $\chi = 0.57$ N/m bubble buckles. The overpressure required to buckle the bubble is a balance of two things: first, the slope of the surface tension is higher for high stiffness bubbles, which means that for a certain decrease in radius the surface tension will go down more in comparison with low χ bubbles. Secondly, for high χ bubbles, more overpressure is needed to decrease the radius with a certain amount in comparison with low χ, since the stiff shell is able to resist the overpressure. As soon as the bubbles buckle, the stiffness of the bubbles is 0 (equilibrium surface tension is zero, so the slope is also zero). This means that the bubble starts to compress more, which can also be seen in Figure 32, for the $\chi = 1.4$ N/m and $\chi = 4.9$ N/m at high overpressure.

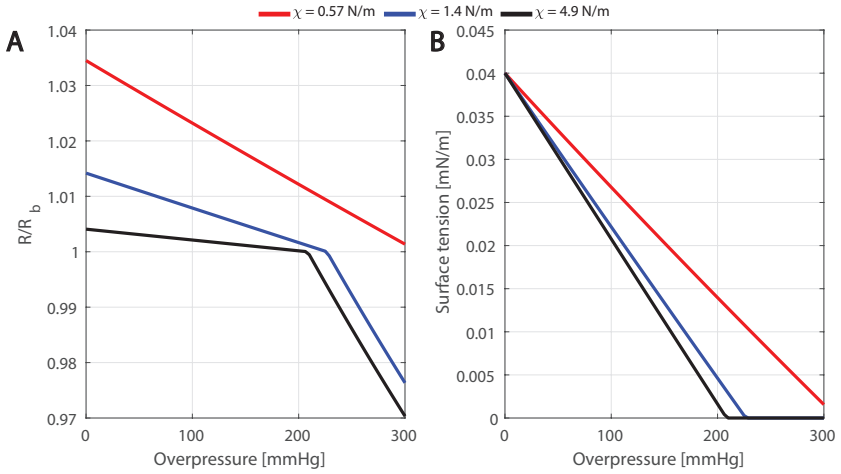

Figure 32: **Normalized radius and surface tension of the different bubble types as function of overpressure. A:** Bubble radius normalized with the buckling radius (Equation 17) of the bubbles versus overpressure. **B:** Initial surface tension versus overpressure. All bubbles start out with the same initial surface tension. The $\chi = 1.4$ N/m and $\chi = 4.9$ N/m bubbles reach zero surface tension before the $\chi = 0.57$ N/m.

Figure 33 shows the CCoS values calculated from the simulations of Figure 31. The increase of CCoS of all bubbles is higher than the increase of the subharmonic mean power, since a decrease in the fundamental also causes the CCoS to increase. The peak of the CCoS of high stiffness bubbles is higher and occurs before the peak of the low stiffness bubble. This is also what is observed in the measured results. The simulations do not take into account attenuation. In the results, the changing of the attenuation spectra of the bubbles due to overpressure, which has an effect on both the fundamental and the subharmonic, changes the amplitude of the measured CCoS, which explains

part of the difference with the simulations.

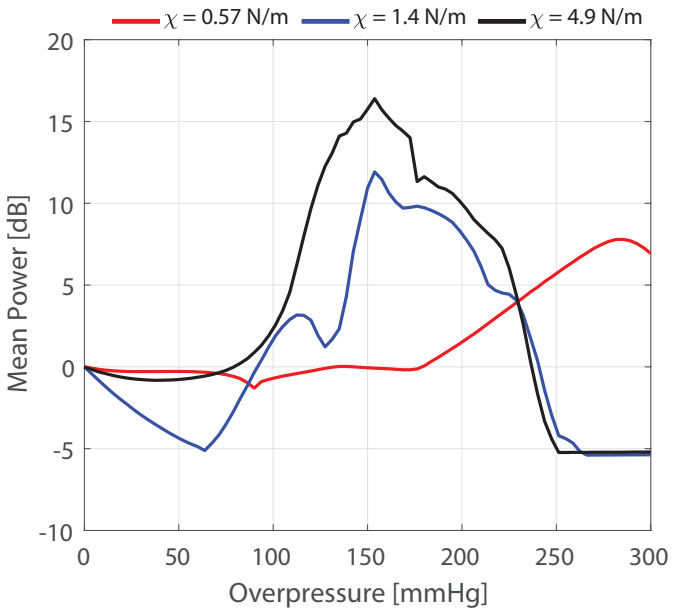

Figure 33: **CCoS of the simulations of the three different bubble types as function of overpressure.** The CCoS of both the high stiffness bubbles peaks higher, and at lower overpressure than the CCoS of the low stiffness bubbles. The simulations show similarities with Figure 30), since both the PA bubbles show an increase in CCoS before the non-PA bubbles. The simulations do not predict a strong increase in the fundamental, as seen in Figure 28, hence the amplitude difference between the $\chi = 1.4$ N/m bubbles and the $\chi = 4.9$ N/m bubbles in Figure 30.

Figure 34 shows the simulated surface tensions of the bubbles according to both Marmottants model (A) and the measured surface tension curves by van Elburg.[18] These simulations show that the surface tension curves stiffer bubbles ($\chi = 1.4$ N/m bubbles and the $\chi = 4.9$ N/m) are almost identical, while the curve of the $\chi = 0.57$ N/m differs a lot with the stiffer bubbles.

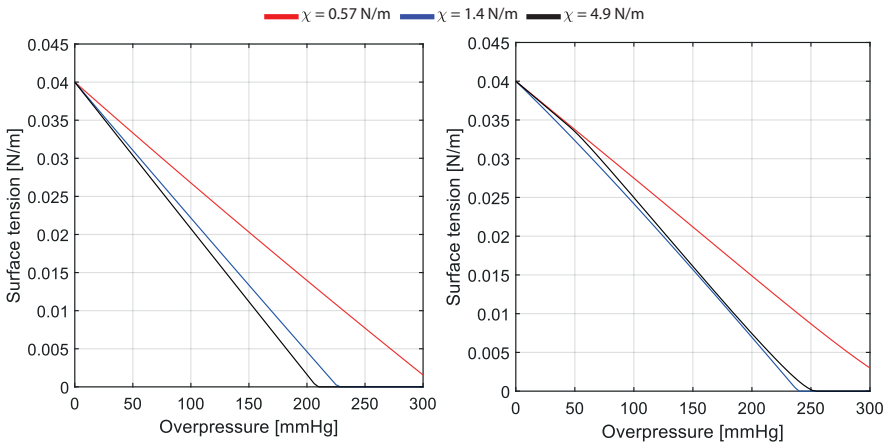

Figure 34: **Simulated surface tensions according to the Marmottant model and surface tension curves. A:** Marmottant model. **B:** Measured surface tension curves.

The initial surface tension has a large effect on both the fundamental and subharmonic response of the bubbles. This is shown in Figure 35, where in A and B the mean fundamental and subharmonic responses of $\chi = 4.9$ N/m bubbles are plotted for a range of initial surface tensions, normalized with with the mean fundamental power at atmospheric pressure. For these bubbles, increasing the initial surface tension causes the individual curves to shift to the right. This can by explained by the fact that increasing the initial surface tension means that more overpressure is required to compress the bubble to the buckling radius. To investigate if the initial surface tension is the sole cause of the shift in the fundamental and subharmonic, the equilibrium overpressure at which the different initial surface tension bubbles buckle is calculated using Equations 6 and 8:

$$P_{eq} = P_0 + \frac{2\chi}{R}\left(\frac{R_b^2}{R_b^2} - 1\right) + P_b, \tag{18}$$

and

$$P_{eq} = \left(P_0 + \frac{2\sigma(R_0)}{R_0}\right)\left(\frac{R_0}{R_b}\right)^{-3\kappa}. \tag{19}$$

If Equation 18 is substituted into Equation 19, it follows that:

$$P_b = \left(P_0 + \frac{2\sigma(R_0)}{R_0}\right)\left(\frac{R_0}{R_b}\right)^{-3\kappa}. \tag{20}$$

From Equation 17 follows that

$$\frac{R_0}{R_b} = \frac{R_0}{R_0}\sqrt{1 + \frac{\sigma(R_0)}{\chi}}. \tag{21}$$

Substituting 21 into 20 gives an expression for the overpressure at which the bubble buckles:

$$P_b = \left(P_0 + \frac{\sigma(R_0)}{R_0}\right)\left(1 + \frac{\sigma(R_0)}{\chi}\right)^{-\frac{3\kappa}{2}} - P_0 \tag{22}$$

Instead of plotting the mean fundamental and subharmonic response versus the overpressure, in Figure 35 C and D, the mean fundamental and subharmonic response are plotted versus overpressure minus the expression for the buckling pressure found in equation 22. According to these simulations, for bubbles with identical, high stiffness, it is not the overpressure, but a combination of the overpressure and initial surface tension which determines the shape of the fundamental and subharmonic response, and thus the CCoS. Whenever the initial surface tension is known, the fundamental and subharmonic response as a function of overpressure can be determined. Whenever the fundamental and subharmonic response as function of overpressure is known, the initial surface tension of the bubbles can be determined. The locations of the peak in the subharmonic and CCoS from the experiments can be used to determine the initial surface tension of the bubbles by making use of simulations. Figure 36 shows the effect of changing the initial surface tension for the $\chi = 0.57$ N/m bubbles, where A and B display the mean fundamental and mean subharmonic response plotted versus the overpressure, and C and D the mean fundamental and subharmonic response plotted versus the overpressure minus the buckling pressure, expressed in equation 22.

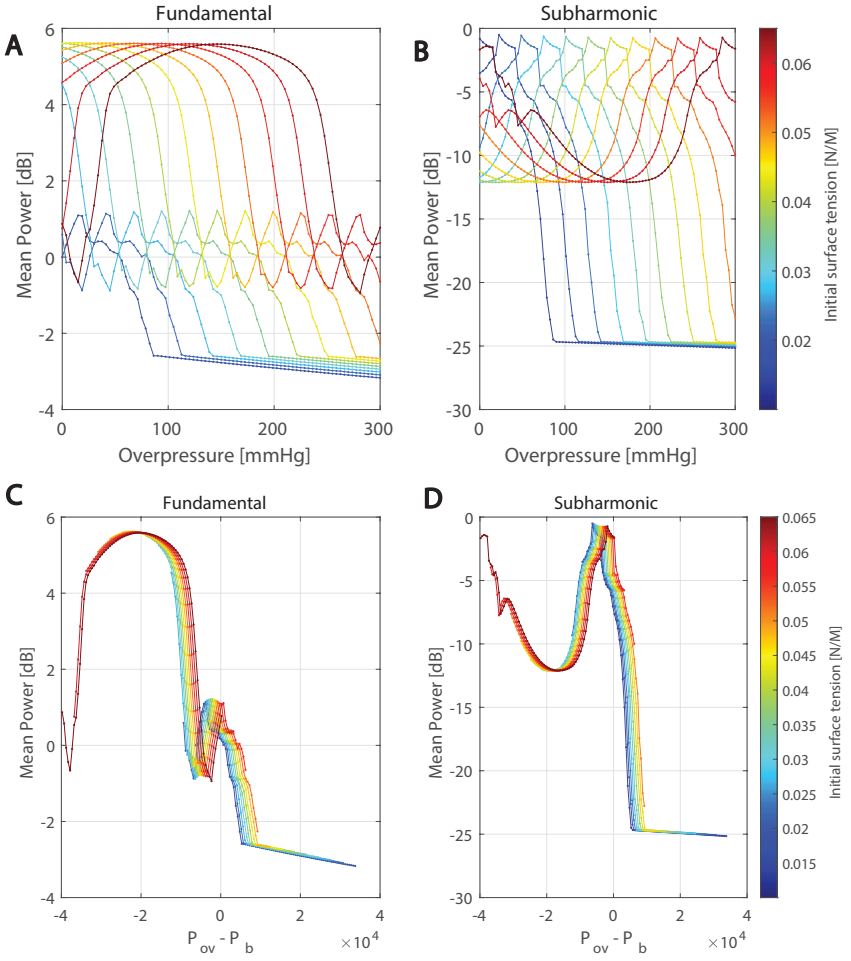

Figure 35: **Simulations of $\chi = 4.9$ N/m bubbles with different initial surface tensions.** R = 3.15 µm, $f_{\text{res}} = 1.7$ MHz, $f_d = 3.4$ MHz. See colorbar for initial surface tension values. **A:** Fundamental mean power vs overpressure. **B:** Subharmonic mean power vs overpressure. **C:** Fundamental mean power vs $\text{P}_{\text{ov}} - \frac{2\sigma(R_0)}{R_0}$. **D:** Fundamental mean power vs $\text{P}_{\text{ov}} - \frac{2\sigma(R_0)}{R_0}$. C and D show a lot of overlap between initial surface tensions.

Figure 36 shows simulations of the $\chi = 0.57$ N/m bubbles. Instead of an almost perfect overlap of all fundamental and subharmonic responses in Figures 35 C and D, Figures 36 C and D show less overlap. The Figure shows that, since there is less overlap between curves, for $\chi = 0.57$ N/m bubbles, there are more factors next to the buckling pressure that have an effect on the shape of the fundamental and subharmonic response. Still, a significant shift causing more overlap is shown..

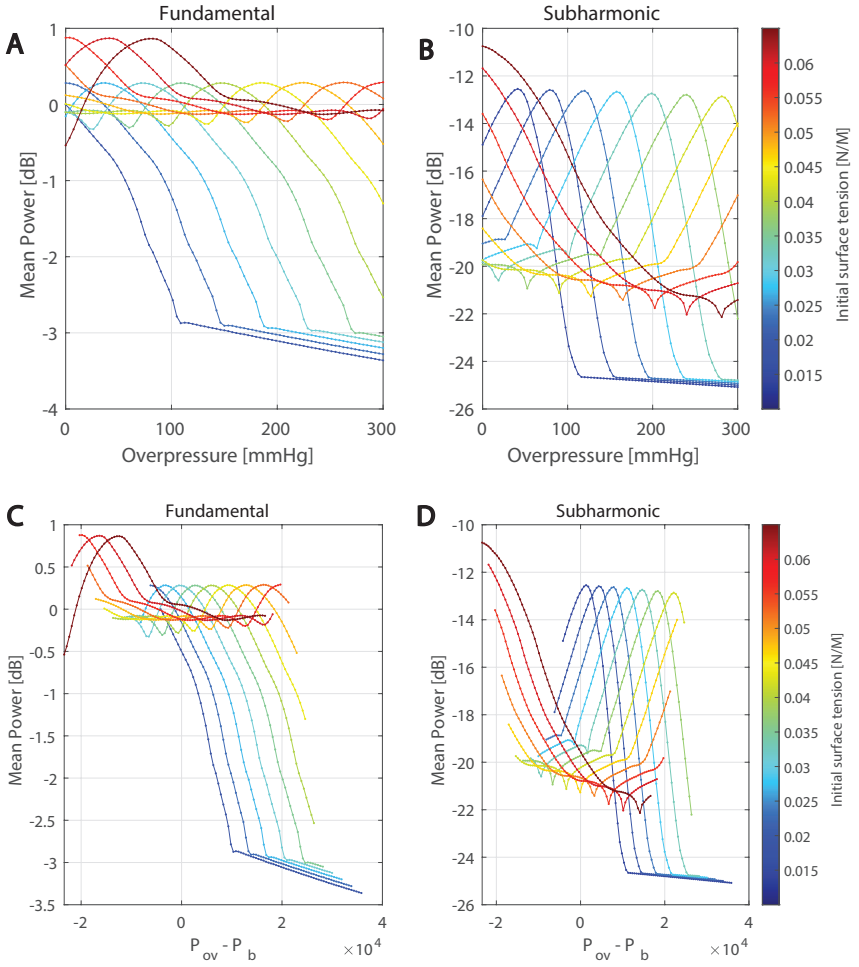

Figure 36: **Simulations of $\chi = 0.57$ N/m bubbles with different initial surface tensions,** R = 2.87 µm, $f_{\text{res}} = 1.7$ MHz, $f_d = 3.4$ MHz. See colorbar for initial surface tension values. **A:** Fundamental mean power vs overpressure. **B:** Subharmonic mean power vs overpressure. **C:** Fundamental mean power vs $\text{P}_{\text{ov}} - \frac{2\sigma(R_0)}{R_0}$. **D:** Fundamental mean power vs $\text{P}_{\text{ov}} - \frac{2\sigma(R_0)}{R_0}$. C and D show less overlap for between initial surface tensions than is shown in Figure 35.

5 Discussion

In this chapter, the results, interesting implications of these results and possible methods to increase the resolution of the proposed method are discussed. To the best of my knowledge, this is the first time the effect of changing the stiffness on the subharmonic response of monodisperse microbubbles has been studied. Different papers provide insight into the subharmonic response of various commercially available polydisperse contrast agents, but in these papers the stiffness of these agents is not the main focus but just a result of the bubble selection. Here, monodisperse bubbles were produced with the goal of changing nothing but the stiffness of the bubbles. In this thesis, multiple variables, such as different bubble concentrations and acoustic pressures resulting from attenuation were tested to gain a better understanding of the fundamental and subharmonic response of all the bubbles. The results of this thesis lay a broad foundation on which future research into the subharmonic acoustical response of monodisperse microbubbles can be based.

This chapter starts with discussing the advantages and disadvantages of each bubble type. Then, the similarities of the observed CCoS of the 30% and 45% PA bubbles are discussed. Methods to improve the resolution in relevant ambient pressure ranges, as well as possible explanations of unexpected bubble behavior are discussed. Finally, brief recommendations for future research are proposed.

5.1 Advantages and disadvantages of each bubble

During this thesis, three different bubble types were used to investigate the fundamental and subharmonic response as a function of overpressure. Each of the different bubbles (0%, 30% and 45% PA) had its own advantages and disadvantages regarding acoustical bubble response, as well as practicality regarding preparation, creation and stability of the bubbles.

The main advantage of the 0% palmitic acid bubbles is that they are easier to produce and store. Adding palmitic acid to the bubbles complicates the production process, since the temperature at which the palmitic acid dissolves into a liquid is significantly higher than the temperature required to make non-palmitic acid bubbles, leading to complications in the bubble maker when temperatures locally drop below the dissolution temperature.

However, the advantages of using palmitic acid bubbles outweigh the disadvantages of using the palmitic acid bubbles for ambient pressure estimation. For example, simulations in Figure 33 show that the addition of palmitic acid decreases the fundamental power more as the ambient pressure goes up, just as it increases the subharmonic power as the ambient pressure goes up. Both these phenomena increase the CCoS. Another major advantage of the palmitic acid bubbles over the non-palmitic acid bubbles is that the palmitic acid bubbles only

attenuate the scattered subharmonic signal weakly, while the 0% palmitic acid bubbles attenuate the scattered subharmonic signal substantially. This means that higher concentrations of PA bubbles can be used in order to amplify both the intensity of the fundamental and subharmonic power over the reflections of surrounding materials. For the 0% palmitic acid bubbles, in deeper sections no subharmonic scattering is observed. This is most likely due to the scattered subharmonic frequencies being almost completely attenuated. The CCoS of the 45% PA bubbles seems to increase more constantly as function of overpressure than the 30% PA bubbles (Figures 29 and 30). This can be explained by the surface tension curves of both bubble types (Figure 6). As the 30% PA bubbles are compressed, the slope of the surface tension changes significantly, while for the 45% PA bubbles, the slope seems to be constant under compression, apart from an almost instant slope change around 35 mN/m. Overall, the 45% PA bubbles seem to perform the best in determining the blood pressure non-invasively, as they share a high resolution with the 30% PA bubbles, and have a constant increase of CCoS as overpressure increases. The behavior of the 45% PA bubbles is also easier to predict with simulations, since simulations of $\chi =$ 4.9 N/m bubbles (Figure 35) show that the shape of the fundamental and subharmonic response is mainly dependent on a combination of the overpressure and buckling pressure of the stiff bubbles.

5.2 Similarities between CCoS of 30% and 45% PA

While the ratio in stiffness between $\chi = 0.57$ N/m to $\chi = 1.4$ N/m and between $\chi = 1.4$ N/m to $\chi = 4.9$ N/m is both around three, the difference in maximum CCoS between the two pairs is clearly not equal. For both the bubbles containing a different molar fraction of palmitic acid, the shape of the CCoS curve is very similar: the overpressure at which the CCoS starts to increase, as well as the slope with which the CCoS increases seems to be equal (Figure 29). The difference between the palmitic acid bubbles and the bubble without palmitic acid is substantial. Even though all bubbles seem to have an equal initial surface tension of about 40 mN/m, the CCoS of the palmitic acid bubbles peaks at lower overpressures than the CCoS of the non-palmitic acid bubbles. The palmitic acid bubbles buckle at lower overpressures than the non-palmitic acid bubble buckle, which is shown by equation 17. This equation shows that stiffer bubbles need to be compressed less in order to reach the buckling radius. The bubble buckling is shown to be related to an increase in subharmonic scattering, and thus an increase in CCoS. This explains why the CCoS of both the palmitic acid bubbles peaks at lower overpressures than the non-palmitic acid bubbles, but it does not explain why the CCoS of $\chi = 1.4$ N/m and $\chi = 4.9$ N/m bubbles looks so similar.

Seeing the difference between $\chi = 1.4$ N/m and $\chi = 4.9$ N/m in combination with the theory about stiffer bubbles scattering more subharmonics, 45% palmitic acid bubbles are expected to scatter more subharmonics. In reality, the amount of subharmonics scattered seem very similar (Figure 34). However,

the simulated surface tension curves of both the Marmottant model and simulating with measured surface tension curves shows that the difference in surface tension for the 30% and 45% palmitic acid curves is minimal. This similarity in surface tension between 30% PA and 45% PA is also shown in Figure 6, where the stiffness is mostly equal, but the 45% PA bubbles have a higher maximum stiffness at $R/R_0 = 1$.

The difference between the red and blue curve in Figure (Figure 34) is larger than the difference between the blue and black curves in the same figure. The stiffness is direclty related to the slope of the surface tension curves in Figure Figure 34. If the bubble is not compressed $A/A_0 = 1$, the slope of the 45% PA curves is steeper than the slope of the 30% PA curve, indicating a higher stiffness. However, as soon as the bubble starts being compressed and the A/A_0 ratio in Marmottants model starts going down, the slope of the 30% PA curve starts to increase, while the slope of the 45% PA curve starts to decrease. For small oscillations around the initial radius, the slope between the 30% and 45% PA bubbles differs, but for large-amplitude oscillations, on average the slopes strongly match. This causes the slopes to become about equal, causing a similar stiffness when compressed, resulting in similar subharmonic scattering and CCoS. However, the 45% PA bubbles show a more consistent increase of CCoS. While the CCoS reaches similar maximum values, the increase of the 30% PA bubbles is less spread out over the entire overpressure range than that of the 45% PA bubbles.

5.3 Tuning the initial surface tension

From the simulations in Figures 35 and 36, it is clear that the dependence of both the scattered fundamental and subharmonic response on the initial surface tension of the bubbles is very large. Increasing the initial surface tension means that the a bubble has to be compressed more in order to buckle. Figures 35 and 36 also show the strong relation between the fundamental and subharmonic and the overpressure depending on the initial surface tension and radius, especially for the high-stiffness bubbles. This behavior is of practical interest because, in theory, if the initial surface tension of the bubbles can be controlled, and therefore the overpressure at which the CCoS peaks can be controlled. This would mean that for specific applications, bubbles could be created and handled in such a way that the initial surface tension would match the exact initial surface tension required for the application. For example, in order to diagnose portal hypertension the diagnostic method needs to have a high resolution between the overpressures of 90 and 110 mmHg.[12] For this application, a CCoS with a high increase over a small range of pressures (i.e. the best performing $\chi = 1.4$ N/m bubble of Figure 30 around 50 mmHg, which could theoretically be shifted to 100 mmHg by increasing the initial surface tension) would be ideal. However, precise control over the initial surface tension has not yet been achieved. A few suggestions to control the initial surface tension could be using a different gas composition inside the bubble, matching or completely not matching the gas composition in blood. Letting

the isoton in which the experiments are performed degas could also affect the initial surface tension, which is then expected to change the ambient pressure at which the CCoS peaks. Finally, the composition of the lipid shell could change the initial surface tension by using more or less densely packed shells.

A more realistic suggestion is to have a device in the clinic that determines the initial surface tension of the bubbles right before they are injected into the patient. For example, a small amount of blood could be drawn and the bubble behaviour could be calibrated inside this blood sample. After calibration and injection of the bubbles in the patient, multiple acquisitions at T2R could be made, resulting in a range of measured CCoS values due to different blood pressures in the patient. This range could be compared to a calibration curve, resulting in an estimation of the blood pressure.

5.4 Behavior of the fundamental response

Figure 28 shows that for greater depths in the container, after an initial decrease, the fundamental mean power starts to increase to values above that of the mean power values at atmospheric pressure. This trend is not predicted by the single-bubble simulations, and can therefore be attributed to attenuation effects. Examples of this are the changing attenuation spectra as the overpressure increases, as well as a decrease of acoustic pressure due to pulse attenuation.

The increase in fundamental mean power with increasing overpressure is only observed for the two palmitic acid bubble types at depths where the acoustic pressure of the pulse drops below 25 kPa (Figure 27). This suggests that at some overpressure, for an acoustic pressure of around 25 kPa, the bubbles are in resonance with the transmit frequency of 3.4 MHz and attenuate a lot of the scattered signal. As the overpressure starts to increase, the bubble starts to shift off resonance, causing less attenuation of the fundamental. The increase of the fundamental contributes to a lower CCoS. Therefore, investigating the attenuation spectra for different acoustic pressures, frequencies and overpressures would give more insight in this phenomenon. For this, an improved bubble simulator that can simulate the acoustic response of multiple bubbles, including the effect of attenuation, would be very useful.

5.5 The effect of pressure pulsation and blood on microbubble behavior

During the experiments, the ambient pressure was increased gradually over time, from 0 to 200+ mmHg in a time span of around 7 seconds. This was the fastest possible increase with the setup. However, the pressure increase and decrease due to a beating heart in a healthy human occurs on a much shorter timescale (Figure 37). It is unknown how the microbubbles behave under such ambient pressure gradients.

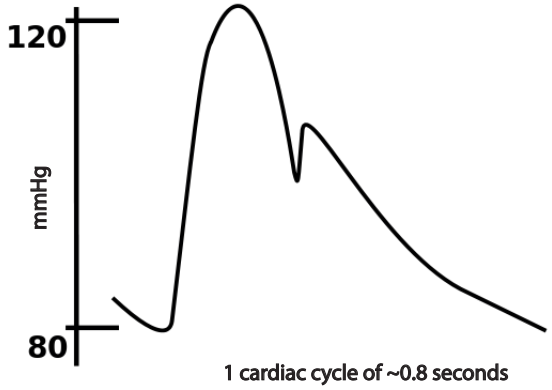

Figure 37: **Arterial blood pressure for a single cardiac cycle** The pressure increase for a single cardiac cycle shows that the timescales at which the pressure increases is multiple orders smaller than the timescale at which the pressure increases in the experiments.

In order to test the bubble response with two different pumping speeds, and thus pressure gradients, the pump speed was lowered by a factor of two. The results are shown in Figure 38, where the orange curve in A took 14 seconds to increase the pressure, instead of 7 seconds of the blue curve. There is a small difference in CCoS of both different pump speeds (Figure 38 B), which could be the result of different pump rates, but could also be the result of other experimental parameters, such as stabilization time. If the bubbles are compressed slower, there is more time for potential gas escaping from the bubbles, which in turn affects the acoustic bubble response. If the shift in CCoS is caused by the different pumping rates, it could be expected that for higher pumping rates (i.e. a human heartbeat) this difference is even larger, since bubbles have less time to stabilize. However, it is not clear how the bubbles would respond for an increase of pump speed up to the timescale of a single heartbeat, since the setup would not allow for this. With slow pumping rates, gas can escape the bubbles. With high pumping rates, the escaping of the gas out of the bubbles is expected to minimize. Because in the simulations there is no escaping of the gas from the bubbles, it can be expected that the simulations can predict the outcome of measurements more accurately at high pumping rates.

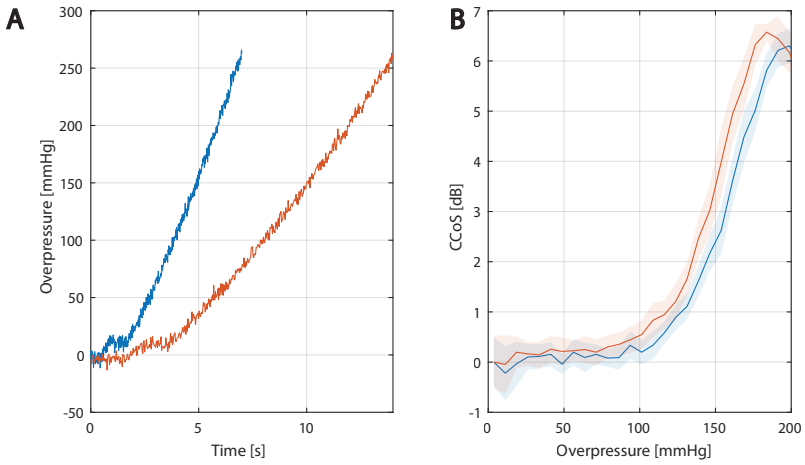

Figure 38: **CCoS for different pump rates. 0% PA, C = 22.500 bubbles/ml. A:** Pressure curves as function of time for two different data sets. Blue increased the pressure in 7 seconds, while orange increased the pressure in 14 seconds. **B:** CCoS of both different data sets. Blue belongs to the blue pressure curve, orange to the orange pressure curve.

Furthermore, a different ambient pressure setup to more accurately mimic the blood pressure in a human body would be an improvement on the overall setup. Being able to program a set of pressure valves to mimic the rapid increase and decrease of pressure in the setup,in combination with using blood, would give insight in how the bubbles respond to rapidly changing pressure gradients. Finally, since the initial surface tension is shown to have a large impact on the CCoS, the effect of degassing or adding extra gas to the isoton, or dissolving the bubbles in blood, on the initial surface tension could be studied.

5.6 Transducer selection

In this thesis, the medically relevant P4-1 ultrasound probe was used to investigate the acoustic bubble response. A medical ultrasound probe was selected to accelerate the translation of the results to a clinical workflow. Also, the P4-1 probe enables transmitting and receiving pulses simultaneously. However, the usage of the P4-1 probe also has its drawbacks. Figure 15 shows the limited bandwidth of the probe. This severely limits the size of the amount of bubbles that can be used. For T2R both the resonance frequency and twice the resonance frequency have to be located within the range of frequencies that can be transmitted and received without too much loss of amplitude response. The probe also limits the acoustic pressures that can be used in experiments. The probe requires a minimal voltage of 1.6 V, which translates to a minimal acoustic pressure of 40 kPa. The presented results in Figure 27 show that the

stiffer bubbles show a higher increase in CCoS at low acoustic pressures. These pressures were only obtained due to attenuation caused by the bubble cloud. The P4-1 probe is a multi-element transducer, which means that it produces large beams with respect to single-element transducers. This prevents the use of small bubble containers, since the entire field has to fit the container in order to minimize scattering from the container itself. A large container has the disadvantage of having a large internal volume, resulting in large bubble clouds, which amplifies the effect of attenuation.

For a better understanding of the acoustic behavior of the bubbles, it is key to reduce the complexity of the system. For this, a single-element transducer can be used. Generally, single-element transducers have a wider bandwidth, which means that a larger range of frequencies can be used in T2R. This would enable more differently sized bubbles to be used in the experiments. Also, a calibrated single-element transducer can transmit acoustic pressures lower than 40 kPa. This would enable investigation of the stiffer bubbles at lower acoustic pressures without relying on attenuation for reaching these low acoustic pressures. Single-element transducers also enable the use of smaller containers (and thus less depth), which results in less acoustic pressure deviation within the measurement volume and reduces the effect of attenuation. However, the reduce the depth of the container, a material for the windows that does not interfere with the bubble signal while maintaining the ability to withstand overpressures above 200 mmHg has to be found. A smaller container is also expected to reduce reduce the effect of variation of the local bubble concentration. With the bubbles confined into a smaller volume, there is less room cause substantial local bubble concentration differences, which is expected to lower the resolution ambient pressure estimations. Single-element transducers also enable performing both attenuation and scattering measurements at the same time. This would give valuable insight in, for example, the behavior of the fundamental observed in Figure 28. The currently expected explanation for this behaviour, the changing of the attenuation spectra as function of ambient and acoustic pressure, could then be tested while the scattering measurements are also performed.

6 Conclusion

The introduced CCoS shows to be a promising variable to make pressure estimations using the acoustic response of monodisperse microbubbles, since it enables pressure estimation with a single T2R acquisition, comparing the fundamental and subharmonic acoustic response. The CCoS was investigated for overpressures ranging from 0 mmHg to 200 mmHg. In this overpressure window, the 0% PA bubbles showed a weak increase of CCoS due to attenuation of the scattered subharmonic. At low concentrations, the CCoS of the 0% PA bubbles reached values just below 2 dB, with a resolution of $\pm$13.37 mmHg, while at high concentrations the CCoS remained negative. At the same specific depth in the container, both the stiffer bubbles (30% and 45% PA) show maximum CCoS values between 4 and 6 dB, with similar slopes of the CCoS curves and an average resolution between $\pm$9.16 and $\pm$9.68 mmHg. At low acoustic pressures (¡25 kPa) the maximum CCoS of both the palmitic acid bubbles increased significantly. The CCoS of the 30% PA bubbles reached a maximum of 11.8 dB, while the CCoS of the 45% bubbles reached an increase of 7.7 dB. At these maxima, both a strong decrease of the fundamental, as a strong increase of the subharmonic, affected the CCoS. Results show that stiff bubbles containing high molar fraction palmitic acid are excellent sensors for ambient pressure estimation, especially compared to non-stiff bubbles. Unlike non-stiff bubbles, stiff bubbles can be used in high concentrations, increasing the intensity of the scattered signal even more.

However, ambient pressure estimation with monodisperse bubbles is complicated by a range of factors, namely variation in local bubble concentration and variation in initial surface tension, attenuation, shifting resonance curves due to attenuation and overpressure. The initial surface tension, an unknown factor before measuring, plays an important role in the shape of the CCoS curves. For stiff bubbles, it is the ambient pressure and buckling pressure, mainly dependent on the initial surface tension and radius, which determines the subharmonic response, in turn affecting the CCoS.

Using the CCoS of palmitic acid monodisperse microbubbles measured at low acoustic pressures as a method to estimate local blood pressures in a human body shows promising results and, if resolution can be improved, might be a clinically viable alternative to current methods. However, further research to improve the resolution of the ambient pressure estimation is required.

7 References

[1] A. F. Connors, "The effectiveness of right heart catheterization in the initial care of critically ill patients. SUPPORT investigators," *JAMA: The Journal of the American Medical Association*, vol. 276, pp. 889–897, sep 1996.

[2] M. M. H. et al, "Complications of right heart catheterization procedures in patients with pulmonary hypertension in experienced centers," *Journal of the American College of Cardiology*, vol. 48, pp. 2546–2552, dec 2006.

[3] F. Forsberg, J.-B. Liu, W. Shi, J. Furuse, M. Shimizu, and B. Goldberg, "In vivo pressure estimation using subharmonic contrast microbubble signals: proof of concept," *IEEE Transactions on Ultrasonics, Ferroelectrics and Frequency Control*, vol. 52, pp. 581–583, apr 2005.

[4] P. Frinking, T. Segers, Y. Luan, and F. Tranquart, "Three decades of ultrasound contrast agents: A review of the past, present and future improvements," *Ultrasound in Medicine Biology*, vol. 46, no. 4, pp. 892–908, 2020.

[5] M. Schneider, "Characteristics of sonovue™," *Echocardiography*, vol. 16, no. s1, pp. 743–746, 1999.

[6] P. C. Sontum, "Physicochemical characteristics of sonazoid™, a new contrast agent for ultrasound imaging," *Ultrasound in Medicine Biology*, vol. 34, no. 5, pp. 824–833, 2008.

[7] M. M. F. Ferraioli Giovanna, "Contrast-enhanced ultrasonography of the liver using sonovue," *Ultrasonography*, vol. 37, no. 1, pp. 25–35, 2018.

[8] W. T. Shi and F. Forsberg, "Ultrasonic characterization of the nonlinear properties of contrast microbubbles," *Ultrasound in Medicine & Biology*, vol. 26, pp. 93–104, jan 2000.

[9] W. Shi, F. Forsberg, J. Raichlen, L. Needleman, and B. Goldberg, "Pressure dependence of subharmonic signals from contrast microbubbles," *Ultrasound in Medicine & Biology*, vol. 25, pp. 275–283, feb 1999.

[10] P. A. Frinking, E. Gaud, J. Brochot, and M. Arditi, "Subharmonic scattering of phospholipid-shell microbubbles at low acoustic pressure amplitudes," *IEEE Transactions on Ultrasonics, Ferroelectrics and Frequency Control*, vol. 57, pp. 1762–1771, aug 2010.

[11] F. Li, D. Li, and F. Yan, "Improvement of detection sensitivity of microbubbles as sensors to detect ambient pressure," *Sensors*, vol. 18, p. 4083, nov 2018.

[12] C. Tremblay-Darveau, "Measuring absolute blood pressure using microbubbles," *Ultrasound in medicine and bioloigy*, vol. 40, pp. P775–787, Apr. 2014.

[13] P. Marmottant, S. van der Meer, M. Emmer, M. Versluis, N. de Jong, S. Hilgenfeldt, and D. Lohse, "A model for large amplitude oscillations of coated bubbles accounting for buckling and rupture," *The Journal of the Acoustical Society of America*, vol. 118, no. 6, pp. 3499–3505, 2005.

[14] T. Segers, L. de Rond, N. de Jong, M. Borden, and M. Versluis, "Stability of monodisperse phospholipid-coated microbubbles formed by flow-focusing at high production rates," *Langmuir*, vol. 32, no. 16, pp. 3937–3944, 2016. PMID: 27006083.

[15] T. Segers, D. Lohse, M. Versluis, and P. Frinking, "Universal equations for the coalescence probability and long-term size stability of phospholipid-coated monodisperse microbubbles formed by flow focusing," *Langmuir*, vol. 33, no. 39, pp. 10329–10339, 2017. PMID: 28872315.

[16] T. Segers, E. Gaud, M. Versluis, and P. Frinking, "High-precision acoustic measurements of the nonlinear dilatational elasticity of phospholipid coated monodisperse microbubbles," *Soft Matter*, vol. 14, pp. 9550–9561, 2018.

[17] K. Hac-Wydro, K. Jedrzejek, and P. Dynarowicz-Łatka, "Effect of saturation degree on the interactions between fatty acids and phosphatidylcholines in binary and ternary langmuir monolayers," *Colloids and Surfaces B: Biointerfaces*, vol. 72, no. 1, pp. 101–111, 2009.

[18] B. van Elburg, "The effect of palmitic acid on microbubbles." 2021.

[19] J. Sijl, B. Dollet, M. Overvelde, V. Garbin, T. Rozendal, N. de Jong, D. Lohse, and M. Versluis, "Subharmonic behavior of phospholipid-coated ultrasound contrast agent microbubbles," *The Journal of the Acoustical Society of America*, vol. 128, pp. 3239–3252, nov 2010.

[20] J. Chomas, P. Dayton, D. May, and K. Ferrara, "Nondestructive subharmonic imaging," *IEEE Transactions on Ultrasonics, Ferroelectrics, and Frequency Control*, vol. 49, no. 7, pp. 883–892, 2002.

[21] A. Katiyar, K. Sarkar, and F. Forsberg, "Modeling subharmonic response from contrast microbubbles as a function of ambient static pressure," *The Journal of the Acoustical Society of America*, vol. 129, no. 4, pp. 2325–2335, 2011.

[22] J. Sijl, M. Overvelde, B. Dollet, V. Garbin, N. de Jong, D. Lohse, and M. Versluis, ""compression-only" behavior: A second-order nonlinear response of ultrasound contrast agent microbubbles," *The Journal of the Acoustical Society of America*, vol. 129, no. 4, pp. 1729–1739, 2011.

[23] T. Segers, A. Lassus, P. Bussat, E. Gaud, and P. Frinking, "Improved coalescence stability of monodisperse phospholipid-coated microbubbles formed by flow-focusing at elevated temperatures," *Lab on a Chip*, vol. 19, no. 1, pp. 158–167, 2019.

[24] T. Segers, E. Gaud, G. Casqueiro, A. Lassus, M. Versluis, and P. Frinking, "Foam-free monodisperse lipid-coated ultrasound contrast agent synthesis by flow-focusing through multi-gas-component microbubble stabilization," *Applied Physics Letters*, vol. 116, p. 173701, apr 2020.

[25] T. Segers, P. Kruizinga, M. P. Kok, G. Lajoinie, N. de Jong, and M. Versluis, "Monodisperse versus polydisperse ultrasound contrast agents: Nonlinear response, sensitivity, and deep tissue imaging potential," *Ultrasound in Medicine Biology*, vol. 44, no. 7, pp. 1482–1492, 2018.

[26] A. Prosperetti, "Thermal effects and damping mechanisms in the forced radial oscillations of gas bubbles in liquids," *The Journal of the Acoustical Society of America*, vol. 61, no. 1, pp. 17–27, 1977.